


5-2014

Phase Transformation in Monolayer Molybdenum Disulphide with and without Defects under Tension Predicted by Atomistic Simulations

Khanh Quoc Dang
University of Arkansas, Fayetteville

Follow this and additional works at: <http://scholarworks.uark.edu/etd>

 Part of the [Polymer and Organic Materials Commons](#), and the [Tribology Commons](#)

Recommended Citation

Dang, Khanh Quoc, "Phase Transformation in Monolayer Molybdenum Disulphide with and without Defects under Tension Predicted by Atomistic Simulations" (2014). *Theses and Dissertations*. 2300.
<http://scholarworks.uark.edu/etd/2300>

This Thesis is brought to you for free and open access by ScholarWorks@UARK. It has been accepted for inclusion in Theses and Dissertations by an authorized administrator of ScholarWorks@UARK. For more information, please contact scholar@uark.edu, ccmiddle@uark.edu.

Phase Transformation in Monolayer Molybdenum Disulphide (MoS_2) with and without Defects
under Tension Predicted by Atomistic Simulations

Phase Transformation in Monolayer Molybdenum Disulphide (MoS₂) with and without Defects
under Tension Predicted by Atomistic Simulations

A thesis submitted in partial fulfillment
of the requirements for the degree of
Master of Science in Mechanical Engineering

by

Khanh Dang
University of Arkansas
Bachelor of Science in Mechanical Engineering, 2012

May 2014
University of Arkansas

This thesis is approved for recommendation to the Graduate Council.

Dr. Douglas E. Spearot
Thesis Director

Dr. Ajay P. Malshe
Committee Member

Dr. Paul C. Millett
Committee Member

ABSTRACT

In addition to its use as a solid lubricant, molybdenum disulphide (MoS_2) has gained recent attention as a possible substitute for silicon as it is increasingly difficult to keep shrinking down electronic devices made of silicon, the conventional electronic material. When thinned down to atomic thickness, monolayer MoS_2 possesses very unique and promising electronic and electrical properties. Unlike electronic and electrical properties, knowledge of the mechanical properties and role of structural defects on these properties of monolayer MoS_2 is unexplored. For this thesis, the two main objectives are (1) to gain insight about the failure mechanism of monolayer MoS_2 by modeling nanoindentation performed on suspended free standing membrane with comparison to experiment and (2) to explore the influence of structural defects on the mechanical properties of monolayer MoS_2 by modelling monolayer MoS_2 membranes with defects and simulating the same nanoindentation process as in part (1). It is shown that the force required for fracture of the MoS_2 monolayer increases with increasing indenter diameter. This relationship and the magnitudes of the breaking forces computed in this work are consistent with experiments presented in the literature. A phase transformation, caused by an abrupt drop in the S-S intralayer Z dimension, is observed prior to failure during both defect-free and defect-containing membrane simulations. This phase transformation is also observed in uniaxial tension simulations. Analysis suggests that structural defects alter the failure mechanisms of monolayer MoS_2 and thus reduce its mechanical performance. For point defects, the phase transformation initiates from accumulated vacancies away from the center of the membrane and accelerates the new phase propagation process. For grain boundary structures, it was found that their fracture strength is independent of the grain boundary energy.

ACKNOWLEDGMENTS

There are many people who helped me through my wonderful and challenging journey as a master student that I want to express my sincere gratitude. First, I would like to thank my research/thesis advisor, Dr. Douglas Spearot for his support and guidance during the past two years. He is not only a great mentor to study from but also a very cool person to hang out with. I would also like to thank Dr. Ajay Malshe and Dr Paul Millett to be part of my master thesis committee.

Second, I am also grateful to my colleagues, especially everyone in Dr. Spearot's research group. Shawn and James have had patience and answered all of the most naïve questions about work related to MoS₂ and LAMMPS. Many of my ideas and algorithms are from interesting conversations and discussions with you guys.

Last but not least, I would like to thank my family and friends especially my parents and girlfriend who always stay alongside and support me through all the hardship during my time as a master student.

This research was supported by the National Science Foundation under grant CMMI #100912. Atomistic simulations in this work were performed at the Arkansas High Performance Computing Center, supported in part by the National Science Foundation via grant MRI-R2 #0959124 (Razor).

DEDICATION

For my parents and girlfriend, those who I love the most.

TABLE OF CONTENTS

ABSTRACT.....	ii
ACKNOWLEDGEMENTS.....	iii
DEDICATION.....	iv
LIST OF FIGURES.....	vii
LIST OF TABLES.....	x
CHAPTER 1: INTRODUCTION.....	1
1.1 Moore’s law.....	1
1.2 2-Dimensional (2D) materials.....	1
1.2.1 Introduction.....	1
1.2.2 Graphene as the favorite 2D material.....	2
1.3 Molybdenum disulfide (MoS ₂).....	4
1.3.1 Bulk MoS ₂	4
1.3.2 Monolayer MoS ₂	5
1.4 Thesis objectives.....	15
CHAPTER 2: BACKGROUND.....	17
2.1 Atomistic simulations.....	17
2.2 Molecular dynamics simulations.....	21
2.3 Molecular statics.....	24
2.4 Interatomic potential.....	28
2.4.1 Introduction.....	28
2.4.2 MoS ₂ interatomic potential.....	29
2.5 Atomistic simulations of nanoindentation.....	31
CHAPTER 3: SIMULATION AND CHARACTERIZATION OF NANOINDENTATION ON PERFECT 2D MEMBRANE.....	33
3.1 Simulation methodology.....	33
3.2 Force-displacement curve.....	36
3.2.1 Role of membrane shape.....	36
3.2.2 Role of indenter and membrane sizes.....	37

3.2.3 Role of indenter speed	41
3.3 Phase transformation	42
CHAPTER 4. SIMULATION AND CHARACTERIZATION OF NANOINDENTATION ON FREESTANDING MoS_2 MEMBRANES WITH DEFECTS	49
4.1 Simulation method	51
4.1.1 Point defects	51
4.1.2 Grain boundary structures	53
4.2 Effect of monosulfur vacancy on mechanical behaviors of monolayer MoS_2	54
4.3 Effect of different 60° grain boundary structures on mechanical behaviors of monolayer MoS_2	60
CHAPTER 5: CONCLUSION	70
5.1 Summary	70
5.2 Recommendations for future work.....	71
REFERENCES	72

LIST OF FIGURES

Figure 1.1 All graphitic forms including 0D bucky balls, 1D nanotubes, 2D graphene, and 3 D graphite [24].....	3
Figure 1.2 Hexagonal crystal structure of MoS ₂ [34]. The zigzag direction is along the X axis, while the armchair direction is along the Y axis.....	5
Figure 1.3 Strain dependence of band gap energies of monolayer MoS ₂ [48]	7
Figure 1.4 Experimental nanoindentation on suspended free standing membrane of monolayer MoS ₂ [50].....	8
Figure 1.5 Energies of grain boundaries as functions of tilt angles, starting from either armchair (AC) or from zigzag (ZZ) [61].....	12
Figure 1.6 60° tilt grain boundary structures of monolayer MoS ₂ predicted and observed by Zhou <i>et al.</i> [62].....	13
Figure 1.7 60° tilt grain boundary structures of monolayer MoS ₂ predicted and observed by Enyashin <i>et al.</i> [63].....	14
Figure 2.1 Periodic boundary conditions in two dimensions.....	19
Figure 2.2 Graphical illustration of steepest descent method [76].	27
Figure 2.3 Graphical illustration of conjugate gradient method [76].	27
Figure 3.1 Monolayer MoS ₂ membrane with fixed boundary condition to mimic experimental settings a) Top view. b) Top view zoom-in. c) Side view zoom-in.....	33
Figure 3.1 Monolayer MoS ₂ membrane with fixed boundary condition to mimic experimental settings. Blue atoms are S, red atoms are Mo. a) Top view. b) Top view zoom-in. c) Side view zoom-in	33
Figure 3.2 A typical force – displacement curve for nanoindentation on suspended circular monolayer MoS ₂ sheets with a diameter of 200 nm and an indenter diameter of 40 nm.	36
Figure 3.3 Breaking force as a function of indenter diameter for nanoindentation on suspended circular single layer MoS ₂ sheets with different membrane diameters.....	38
Figure 3.4 Force – displacement curve for nanoindentation on suspended circular monolayer MoS ₂ sheets with an indenter diameter of 40 nm and different membrane diameters.	39

Figure 3.5 Force – displacement curve for nanoindentation on suspended circular monolayer MoS ₂ sheets with a diameter of 200 nm and an indenter diameter of 20 nm at different indenter speed.	40
Figure 3.6 Top view of the phase transformation colored by S potential energy (the membrane and indenter diameters are 150 and 40 nm, respectively). Atoms colored blue have undergone the phase transformation.	41
Figure 3.7 Hexagonal lattice units of Mo, S in the new phase compared to original structure	42
Figure 3.8 Top view of the phase transformation initiation. In the left figure, Mo atoms are removed, coloring S atoms by potential energy; a pair of S atoms is marked by the red arrow. In the right figure, S atoms are removed, coloring Mo atoms by potential energy; the corresponding 4 Mo atoms are marked by the blue rhombus.	43
Figure 3.9 S-S intralayer distance versus simulation time step for different membrane diameters using the same indenter diameter of 40 nm.	44
Figure 3.10 Comparison of the hexagonal lattice units between original and new phases indicating the magnitude and the direction of the shear distortion [88], [89].	46
Figure 3.11 Propagation of the phase transformation during uniaxial tension. The expanded view allows for visual analysis as a black line is drawn between the original phases (green) across the new phase (blue) illustrating the distortion of the lattice in the zig-zag direction [88], [89].	46
Figure 4.1 Different point defects in monolayer MoS ₂ observed via scanning transmission electron microscopy by Zhou et al. [62].	48
Figure 4.2 Top view of monolayer MoS ₂ free standing membrane with membrane diameter of 100 nm. The central red circle is the removal area whose diameter is 20 nm.	50
Figure 4.3 Top view of the membrane with monosulfur vacancies colored by S potential energy during the nanoindentation (the membrane and point defect ratios are 100 nm and 0.01, respectively). Atoms colored blue are the top S sulfur atom above a sulfur vacancy.	54
Figure 4.4 Force – displacement curve for nanoindentation on suspended circular monolayer MoS ₂ sheets with a diameter of 100 nm and point defect ratio of 0.05 with different random delete seeds.	55
Figure 4.5 Top view of the phase transformation initiation in the membrane with a diameter of 100 nm and 0.05 point defect ratio. Mo atoms are removed and S atoms are colored by potential energy in both figures. Atoms colored green are the top S sulfur atom above a sulfur vacancy. A group of 3 vacancies, where the phase transformation initiates from, closest to the center of the membrane is marked by the black circle.	57

Figure 4.6 Top view of the phase transformation initiation in the membrane with a diameter of 200 nm and 0.1 point defect ratio. Mo atoms are removed and S atoms are colored by potential energy in both figures. Atoms colored green are the top S sulfur atom above a sulfur vacancy. Different groups of accumulated vacancies, where the phase transformation initiates from, are marked by the black circles.....	57
Figure 4.7 Force – displacement curve for nanoindentation on suspended circular monolayer MoS ₂ membranes with and without monosulfur vacancies. The diameter of these membranes is 200 nm.	58
Figure 4.8 Grain boundary energies for 60° armchair symmetric tilt grain boundary structures of monolayer MoS ₂ membrane with diameter of 100 nm.....	60
Figure 4.9 Grain boundary energies for 60° zigzag symmetric tilt grain boundary structures of monolayer MoS ₂ membrane with diameter of 100 nm.....	60
Figure 4.10 60° armchair symmetric tilt 4-fold S grain boundary structure of monolayer MoS ₂ corresponding to grain boundary energy of 0.44 eV/Å. Mo atoms are red, while S atoms are blue.....	61
Figure 4.11 60° armchair symmetric tilt Mo-bridge grain boundary structure of monolayer MoS ₂ corresponding to grain boundary energy range from 0.65 to 0.82 eV/Å. Mo atoms are red, while S atoms are blue.....	61
Figure 4.12 60° zigzag symmetric tilt 4/8 grain boundary structure of monolayer MoS ₂ corresponding to grain boundary energy of 0.39 eV/Å. Mo atoms are red, while S atoms are blue.....	62
Figure 4.13 Top view of the phase transformation initiation in 4-fold S grain boundary membrane with diameter of 150 nm. Mo atoms are removed and S atoms are colored by potential energy in both figures. The black box marks 4 S pairs that initiate the phase transformation.	64
Figure 4.14 Top view of the phase transformation propagation process of Mo-bridge (a) and 4-fold S (b) grain boundary membrane with diameter of 100 nm. Mo atoms are removed and S atoms are colored by potential energy in both figures.....	65
Figure 4.15 Top view of the phase transformation initiation in 4/8 ring grain boundary membrane with diameter of 150 nm. Mo atoms are removed and S atoms are colored by potential energy in both figures. The red arrows mark 3 S pairs that initiate the phase transformation.	65
Figure 4.16 Force – displacement curve for nanoindentation on suspended circular monolayer MoS ₂ membranes with and without grain boundary structures. The diameter of these membranes is 200 nm.....	66

LIST OF TABLES

Table 3.1 Number of atoms in monolayer MoS ₂ circular membrane at different membrane diameters	34
Table 3.2 Breaking forces for each simulation in this work. Breaking forces are reported in nN and indenter and membrane diameters are reported in nm.	37
Table 4.1 Table 4.1 The vacancy formation energy ranges for monosulfur vacancy using chemical potential ranges of [-1.4,0] eV [61,62] for different membrane sizes. The membrane diameter is in nm.....	53
Table 4.2 Number of vacancies and breaking forces for membranes with the same diameters of 100 nm and different random delete seeds.	54
Table 4.3 Breaking forces for different membrane sizes and point defect ratios. Breaking forces are reported in nN..	58
Table 4.4 Breaking forces for different membrane sizes and grain boundary structures. Breaking forces are reported in nN.....	64

CHAPTER 1: INTRODUCTION

1.1 Moore's law

Moore's law is the observation that the number of transistors on integrated circuits doubles approximately every 18-24 months [1]. It was first proposed by Gordon E. Moore in 1965 that the number of components on integrated circuits would double each year for the next decade. In 1975, Moore changed the time frame to two years as the rate of growth was slower than his original prediction. Recently, it is increasingly difficult to keep shrinking electronic devices made of silicon, the conventional electronic material. As the gate oxide becomes thinner, the electrons could penetrate through this insulation layer, known as quantum tunneling effect [2]. Since it is impossible to stop electrons from tunneling through thin barriers, either new transistor designs, new novel materials, or both must be found in order to keep up with Moore's prediction. In this thesis, the focus would be the study of new materials in order to continue the scaling down trend.

1.2 2-Dimensional (2D) materials

1.2.1 Introduction

Recently, two dimensional (2D) materials, whose “atomic organization and bond strength along two-dimensions are similar and much stronger than along a third dimension” [3], have gained more attention as a possible substitute for silicon in electronic devices. They can exist in the form of exceptionally thin sheets with a thickness of a few atoms (less than 10) [4] which can satisfy the need for much smaller transistors. Moreover, it is not the size but the dimensional reduction that produces totally different optical and electronic properties compared to their corresponding regular three dimensional (3D) materials. The properties of 2D materials have

been studied and proven to be suitable for several applications such as supercapacitors for rechargeable batteries [5], far-ultraviolet (FUV) light emission screens [6], and gas sensors [7]. Recently, it has been shown that it is possible to stack these individual sheets of 2D materials to generate heterostructures with desired and unique properties, combining from those of the individual layers [8–10]. A detailed overview of the van der Waals heterostructures can be found in [11]. Currently, there are three main classes of two dimensional materials: layered van der Waals solids, layered ionic solids, and nonlayered materials that can be synthesized by different deposition techniques [3]. A more comprehensive review about these 3 classes structures, their exfoliation methods from bulk counterparts, and excellent electronic properties can be found in [3,4,12]. Among these three, layered van der Waals solids are the most well-known class including the most extensively studied 2D material, graphene.

1.2.2 Graphene as the favorite 2D material

Graphene is the 2D form of sp^2 carbon; in other words, it is a monolayer of graphite. Graphene along with other graphitic structures are shown in Figure 1.1. Graphene is one of the stiffest materials, exhibiting a Young's modulus of 1TPa [13], with high thermal [14] and electrical conductivity [15]. A recent study suggests that this Young's modulus varies with strain and could be up to 2.4 TPa for small strain ranges [16]. Graphene exhibits many unusual electronic properties such as quantum Hall effect at room temperature [17,18]. Since its discovery, identification, and characterization in 2004, there has been considerable attention to graphene from both academia and industry resulting in a huge amount of publications related to this material. However, the biggest problem with graphene is that pristine graphene does not have a band gap, which is necessary for semiconducting devices. As a result, graphene field

effect transistors (FETs) have a small current on/off ratio [19], which means it is impossible to turn the current flow off. There have been established methods to artificially reproduce a bandgap in graphene such as surface tuning by introducing dopants [20], lateral confinement [21,22], or uniaxial strain [23]. However, these methods are considered to be quite complex and challenging with current technology. Also, this engineered band gap could reduce the carrier mobility, which affects the desired electronic properties of graphene. Thus, exploring the properties of other 2D materials is an alternative and promising approach that gains more attention recently.

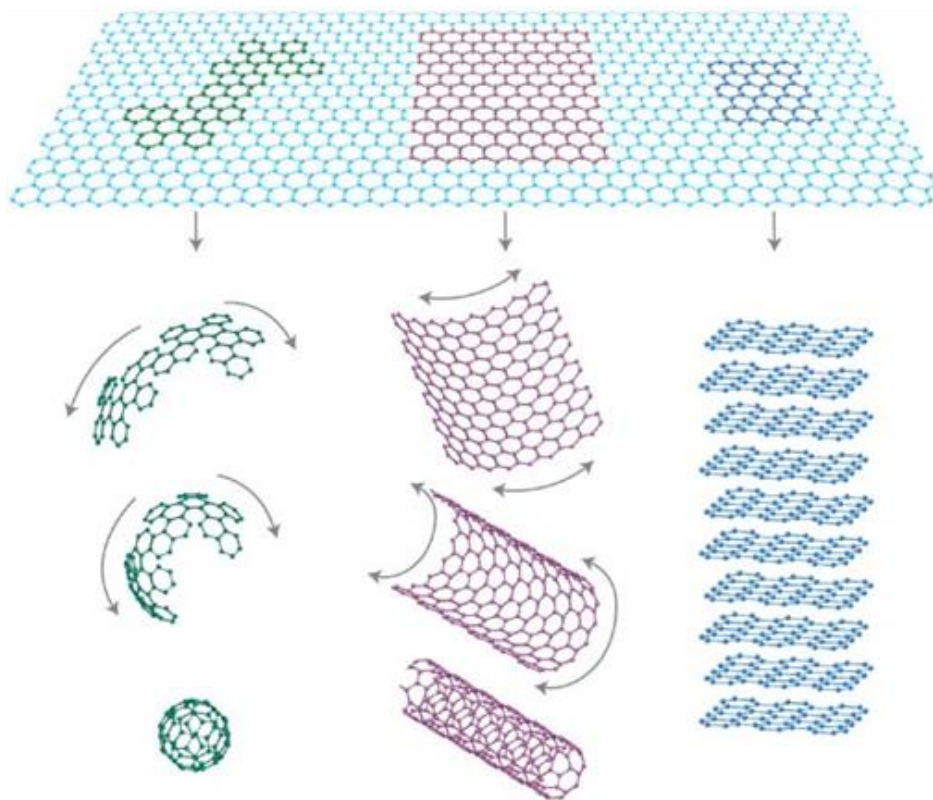


Figure 1.1 All graphitic forms including 0D bucky balls, 1D nanotubes, 2D graphene, and 3 D graphite [24].

The successful isolation and characterization of graphene also opens up new possibilities for research about layered structure materials similar to graphite. Unlike graphene, information and knowledge about most other 2D material properties are inadequate and limited, especially their mechanical properties. Therefore, research about 2D material is a rising and promising field among scientists and research groups. The focus of this thesis is a layered metal dichalcogenide, molybdenum disulfide.

1.3 Molybdenum disulfide (MoS_2)

1.3.1 Bulk MoS_2

“Molybdenum disulfide (MoS_2) is an inorganic compound that has a layered crystal structure where each layer consists of a Sulfur - Molybdenum - Sulfur (S-Mo-S) trilayer” [25,26]. Molybdenum disulfide exists in two crystalline forms, hexagonal and rhombohedral [27]. At one point, the hexagonal, as shown in Figure 1.2, was the only known crystalline form since it was the only form found in molybdenite ores. In 1957, the rhombohedral form was identified in a synthetic material by Bell and Herfert [28]. Both configurations have the same a-axis; the only difference between them is the c-axis. The rhombohedral’s c-axis is 1.5 greater than the one of the hexagonal, which resulting in 3 molecules per unit cell instead of 2 [27]. In this thesis, only hexagonal MoS_2 (h- MoS_2), whose structure is shown in Fig. 2, is studied. There are two different prevalent bonds in the lattice of MoS_2 , covalent interatomic and van der Waals bonds. The covalent interatomic bonds bind together the individual sheets of S and Mo that compose a monolayer of MoS_2 and the van der Waals bonds bind each of the layers together. “The van der Waals bonds between trilayers are relatively weak and break easily during an applied shearing force, which allows the layers to easily slide parallel to each other, resulting in

an extremely low coefficient of friction” [26,29,30]. Another reason for this low coefficient of friction is the distribution of electrons on the constituent atoms [31]. The region around each S atom is positively charged since the nonbonding electrons are concentrated in the middle of each layer. With this positive charge, adjacent layers have a tendency to separate from each other. As a result of this low coefficient of friction, “MoS₂ is widely used as a solid lubricant or as an additive to liquid lubricants providing increased wear resistance” [26,32–34].

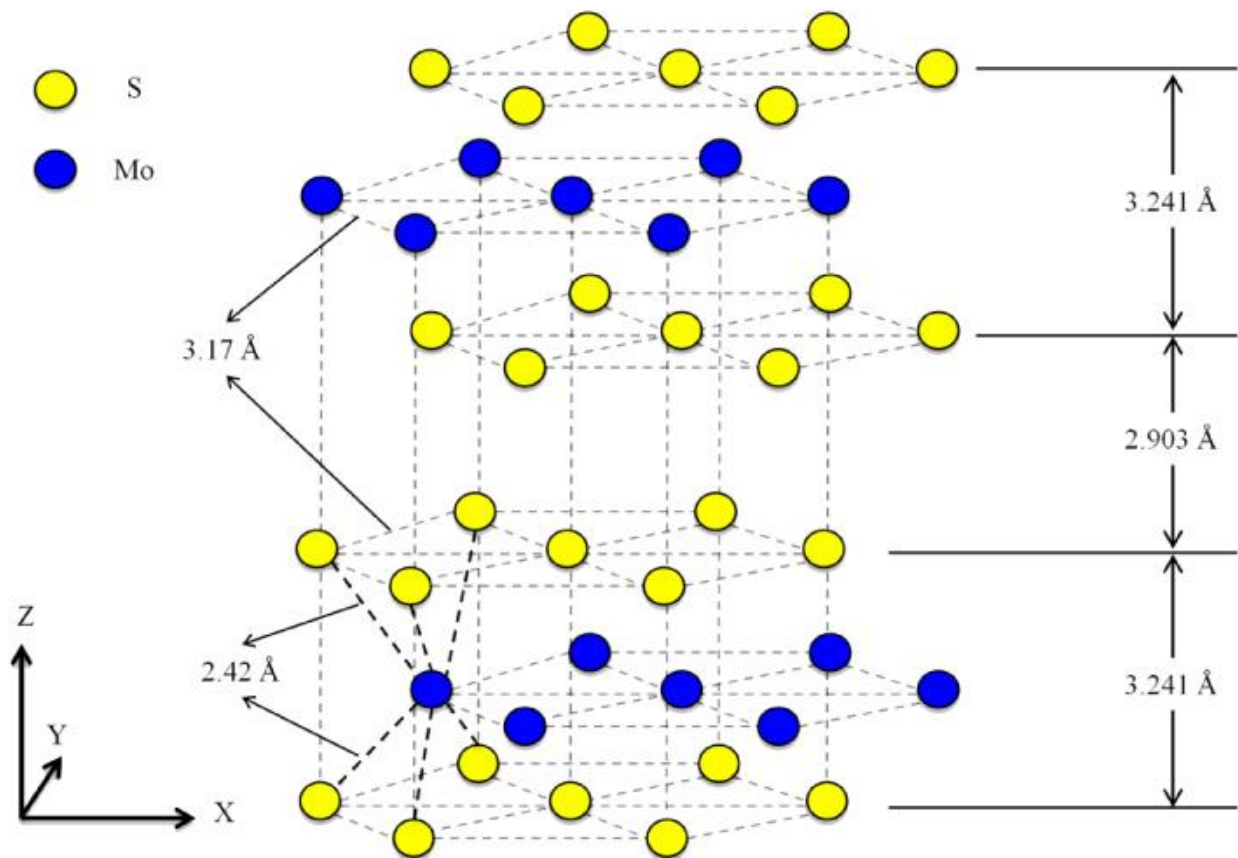


Figure 1.2 Hexagonal crystal structure of MoS₂ [35]. The zigzag direction is along the X axis, while the armchair direction is along the Y axis.

1.3.2 Monolayer MoS₂

Surprisingly, monolayer MoS₂ was first successfully exfoliated in 1986 by intercalation with lithium followed by reaction with water [36]. However, it did not receive much attention until a monolayer MoS₂ based transistor was proposed with a mobility of $200 \text{ cm}^2 \text{ V}^{-1} \text{ s}^{-1}$ at room temperature and high on/off ratios of 1×10^8 [37]. Compared to the absence of band gap in graphene, bulk MoS₂ is an indirect band gap semiconductor. Reducing the number of layers modifies the band structure, resulting in a direct band gap of 1.9 eV for monolayer MoS₂ [38,39]. This contributes to the uniquely high quantum luminescence efficiency suitable for sensing and optoelectronic applications. A more detailed review of the electronic and electrical properties can be found in [3,12]. Based on the unique and promising electronic properties of monolayer MoS₂, several nano optoelectronic structures and devices have been presented recently. Some examples within the last few years are field effect transistor [37], photodetectors [40], phototransistor [41], nanomechanical resonator [42], gas nanosensor [43], small-signal amplifier [44], and integrated circuit [45]. The purpose of this list is not to cover every application but to demonstrate the steady increasing interest in and the potential of monolayer MoS₂ based devices.

Unlike electronic and electrical properties, knowledge of the mechanical properties of monolayer MoS₂ is limited and unexplored. There are three main reasons for the necessity of this knowledge [46]. First, the design and fabrication of monolayer MoS₂ based devices or structures requires the complete knowledge of mechanical properties and responses under deformations. Second, strain is a common variable to engineer when tailoring functional and structural properties of nanomaterials. Third, monolayer MoS₂ is vulnerable to strain due to its monoatomic thickness. Indeed, it is found that monolayer MoS₂ transitions into an indirect band gap semiconductor at around 2 % tensile strain [47–49] and later turns into a metallic material, in terms of conductivity, at 9 % strain [47] as shown in Figure 1.3. Tensile strain also decreases the

optical band gap of about 45 meV/% for monolayer MoS₂ [48]. While the tensile strain reduces the band gap energy; the compressive strain enhances it [49]. These results show that there is a direct relationship between mechanical strain and optoelectronic properties and performances of monolayer MoS₂. Therefore, the full understanding about the mechanical response under deformation of monolayer MoS₂ is crucial before its implementation into electronic devices.

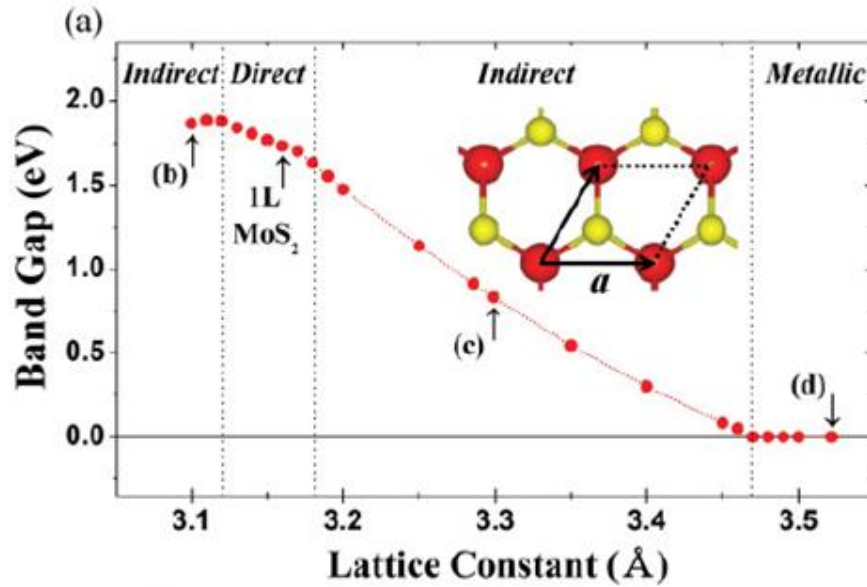


Figure 1.3 Strain dependence of band gap energies of monolayer MoS₂ [49].

In an effort to fulfill this lack of knowledge, there have been several experimental works, computational simulations, or combination of both to study the mechanical properties of monolayer MoS₂. Experimentally, one of the most popular methods to investigate and study the mechanical properties of thin-layer structures is to generate a multiaxial tension by applying nanoindentation on free standing membranes [13,50]. Bertolazzi *et al.* [51] experimentally measured the breaking strength and the in-plane stiffness of a suspended free standing monolayer MoS₂ membrane over circular holes in Si under nanoindentation via atomic force microscopy, as

shown in Figure 1.4. The diameters of the membrane and the indenter are 550 ± 10 and 12 ± 2 nm, respectively. They reported the measured breaking force and corresponding deflection of approximately 200 nN and 50 nm. They found that no plastic deformation occurs during their nanoindentation process since loading and unloading curves generally overlap. Bertolazzi *et al.* [51] also calculated the average stiffness modulus and ultimate strength of 180 ± 60 and 15 ± 3 Nm^{-1} , respectively, which shows that the strength of monolayer MoS_2 is between 6 and 11 % of its stiffness modulus. Based on the typical ratio between the strength and stiffness modulus of defect-free material [52], they suggested that monolayer MoS_2 membranes are mostly defect-free. By comparing the Young's modulus and breaking strength of monolayer MoS_2 with other materials, they affirmed that monolayer MoS_2 is a flexible and strong material that could potentially be implemented into electronic devices.

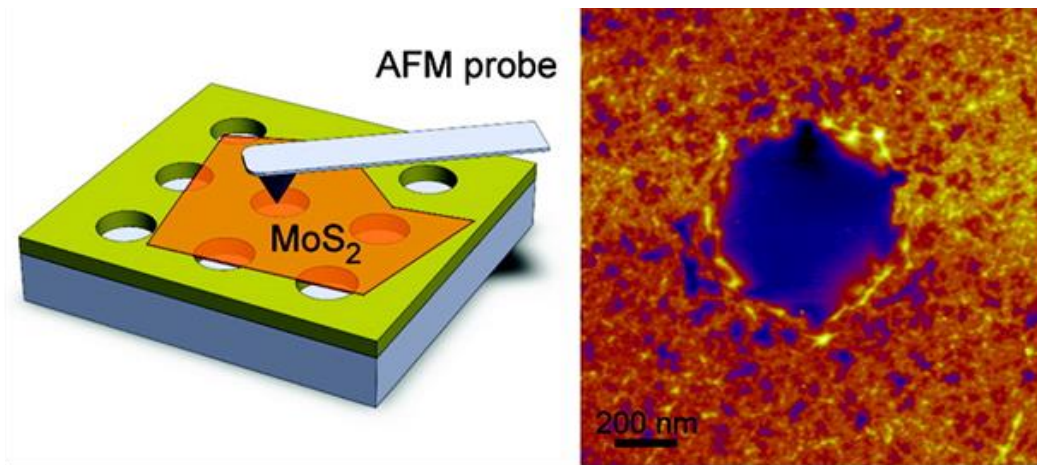


Figure 1.4 Experimental nanoindentation on a suspended free standing membrane of monolayer MoS_2 [51].

Cooper *et al.* [53] developed a multiscale constitutive model to capture the nonlinear elastic behavior of monolayer MoS_2 . They derived a general form via a Taylor series expansion of the elastic strain energy density potential. The 14 independent parameters were determined by

fitting this model to elastic properties computed via different density functional calculations. The model was then employed into a finite element analysis and validated by comparing the simulated result to experimental values of indentation on a suspended circular membrane via atomic force microscopy. They reported that the 95% confidence interval for the experimental breaking force is 1350-1650 nN for the membrane diameter of 500 nm and indenter diameter of 52 nm. The computed ultimate stress and in-plane elastic modulus from this model were 130 and 16.5 Nm^{-1} , respectively, which were in good agreement with Bertolazzi *et al.* [51] experimental results. With this model, Cooper *et al.* [53] bridged the gap between experiment and simulation as well as provide useful model for large scale simulation.

Similarly, Peng and De [46] investigated the structural and elastic properties of nanoribbon structures of monolayer MoS_2 at 0 K under large deformation using density functional theory calculations. They reported the ultimate strengths of 11.9, 12.6, and 15.1 Nm^{-1} corresponding to the ultimate strains of 0.24, 0.37, and 0.26 for armchair, zigzag, and biaxial tensile deformation, respectively. Also, the in-plane elastic modulus was slightly higher in the armchair direction. The results from their simulations suggest that nanoribbon monolayer MoS_2 is softer and could sustain higher strain in the zigzag direction. From the stress strain curves, the 14 independent elastic constant were explicitly determined for potential incorporation into larger scale simulation methods such as finite element analysis. With a relative high ultimate strength and strain, Peng and De [46] suggested monolayer MoS_2 as a potential material for elastic storage applications.

Jiang *et al.* [54] parameterized a bond order potential for Mo-S systems based on the phonon spectrum of monolayer MoS_2 to study the mechanical and thermal properties of monolayer MoS_2 nano ribbons with free edges. This interatomic potential could reproduce the

MoS₂ structure with the Mo-S bond length of 2.3920 Å compared to 2.382 Å from *ab initio* calculation. Using this interatomic potential, Jiang *et al.* [54] showed that both chirality and width of the monolayer MoS₂ ribbons influence the elastic modulus. On the other hand, the thermal conductivity was sensitive to only temperature, not chirality. The results from their molecular dynamics simulation also suggested that increasing tensile strain of the monolayer MoS₂ nanoribbons reduces the thermal conductivity.

Structural defects in monolayer MoS₂ have gained much attention recently. Structural imperfections such as point defects, line defects, and grain boundaries are commonly observed in 2D materials. Unlike the traditional definition, “in 2D materials, grain boundaries are the one-dimensional (1D) interfaces between two domains of materials with different crystallographic orientations” [55]. The point defects could be generated during the growth process [56,57] or by ballistic displacements during imaging characterization such as electron irradiation process in high resolution transmission electron microscopy (HR-TEM) [58,59]. The appearance of these defects can significantly influence the mechanical, optical, thermal, and electrical properties of 2D materials. For example, the presence of defects significantly reduces the failure strain and the intrinsic strength of graphene sheets [60]. The structural defects in 2D materials also provide opportunities for tailoring desired functionalities. An example of this would be the tunable magnetic phases in graphene induced by vacancies [61]. For monolayer MoS₂, the characterization and visualization of the structural defects have been explored both experimentally and computationally.

Komsa *et al.* [62] studied the vacancies in monolayer MoS₂ membrane induced by electron irradiation via dynamical density functional theory simulations. They found that the displacement threshold energy (T_d) for sputtering a bottom S atom from the monolayer MoS₂

membrane is 6.9 eV corresponding to the electron energies of 90 keV. Experimentally, they observed single and double S vacancies (monosulfur vacancies and disulfur vacancies, respectively) in a monolayer MoS₂ sheet under an 80 keV electron beam using HR-TEM. Most of the captured vacancies are single S vacancies in the bottom layer of the membrane since the displacement threshold energy for the top S atom is higher. The calculated relaxed and nonrelaxed vacancy formation energies (E_f) of monosulfur vacancy, which is a missing of a S atom, in the bottom layer of the membrane are 6.6 and 6.9 eV suggesting that the energy is conserved during the fast sputtering process. From supplemental calculations of formation energies for different substitution defects in MoS₂ and observed filling vacancies in the HR-TEM, Komsa *et al.* [62] suggested the potential of electron-beam mediated doping for monolayer MoS₂ to tailor desired properties.

Zou *et al.* [63] manually removed different possible half-planes to predict the symmetric tilt grain boundary structures of monolayer MoS₂. Electronic properties of these structures are then computed via density functional theory calculations. Unlike graphene, grain boundary structures of monolayer MoS₂ are composed of 5-7, 6-8, 4-6 or less stable 4-8 rings. Zou *et al.* [63] reported that the statistical preference of certain grain boundaries structures depend on the local organization of atoms and chemical potentials of the constituent elements. As shown in Figure 1.5, the grain boundary energy is proportional to the tilt angles because of higher dislocation density at large tilt angles. They also found that 60° tilt monolayer MoS₂ interfaces comprise a compact row of homoelemental bonds, Mo-Mo or S-S. In term of the effect on electronic properties of monolayer MoS₂, the band structure for 60° tilt grain boundary showed the delocalized states in one dimension implying the metallic behavior of the grain boundaries.

Zhou et al. [62] experimentally studied the structural defects in monolayer MoS₂ grown by chemical vapor deposition method via scanning transmission electron microscopy. They also performed ab initio calculations to investigate the role of these defects on the electronic properties of monolayer MoS₂. Six different types of point defects are observed in their monolayer MoS₂ sheets, where monosulfur vacancy, denoted as V_s in their article, is frequently spotted in all samples. A more detail description about these point defects can be found in Chapter 4. Their calculations, in agreement with experimental observation, showed that monosulfur vacancy has the lowest formation energy. By plotting the electronic band structures,

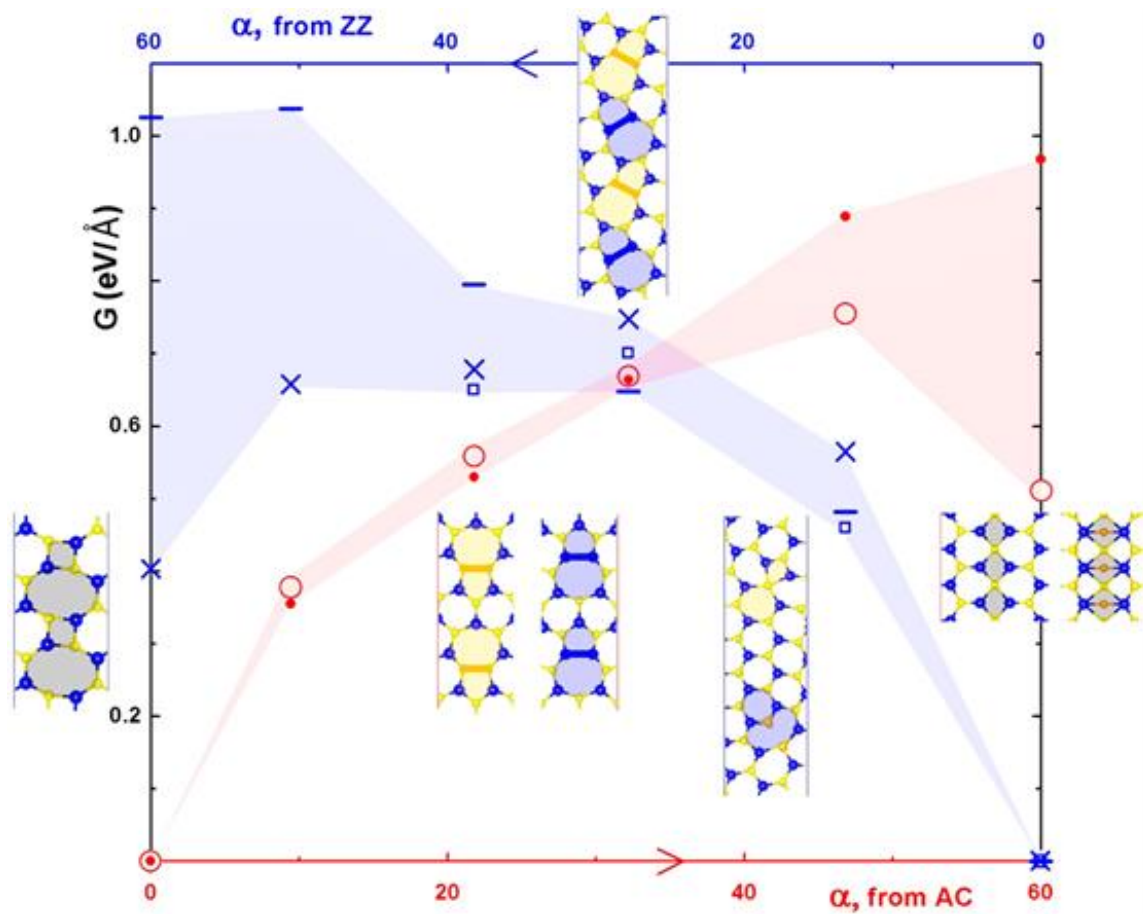


Figure 1.5 Energies of grain boundaries as functions of tilt angles, starting from either armchair (AC) or from zigzag (ZZ) [63].

Zhou *et al.* [62] showed that the appearance of monosulfur and disulfur vacancies affects the electronic properties, reducing the electrical conductance. Using atomic-resolution annular dark field (ADF) imaging on an aberration-corrected scanning transmission electron microscopy (STEM), Zhou *et al.* [64] captured 2 different structures for the 60° monolayer MoS₂ grain boundary: 4-fold coordinated S atoms and 4-fold rings with edge sharing as shown in Figure 1.7. Their density functional calculations showed that while these observed grain boundaries have metallic behavior, the predicted structure 4-8 grain boundary (which is the 4-fold rings with edge sharing with the highest density of kink pairs) only presents a narrow band gap, indicating the potential of tailoring desired electronic properties of monolayer MoS₂ by tuning the grain boundary structures.

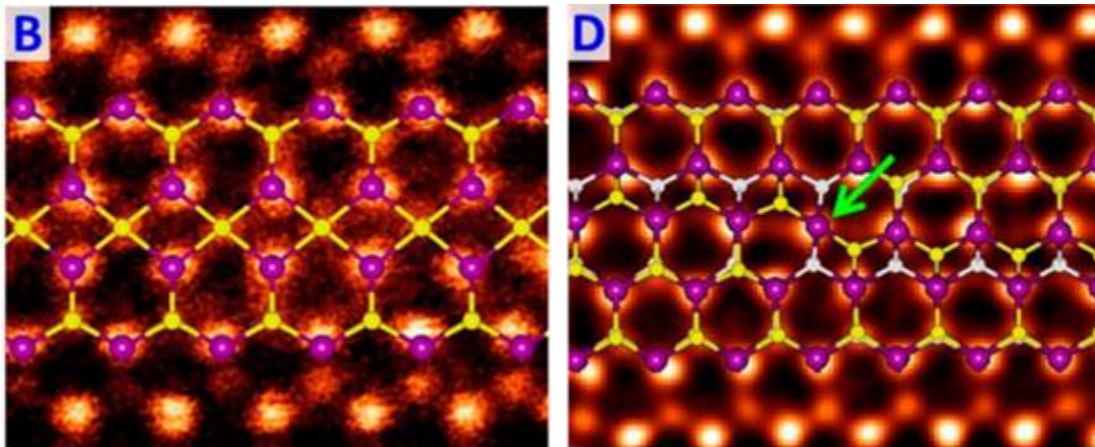


Figure 1.6 60° tilt grain boundary structures of monolayer MoS₂ predicted and observed by Zhou *et al.* [64].

Enyashin *et al.* [65] used density functional theory based tight binding method with molecular dynamics simulations at 300 and 600 K to predict different structures of grain boundaries in monolayer MoS₂. Their experimental transmission electron microscopy images

also confirmed the appearance of the Mo-Mo bonds or S bridge structures between 60° tilt grain boundaries as shown in Figure 1.8. Their calculations also showed there is a new localized trap states near the Fermi level and in the band gap region, indicating the metallic behavior of these grain boundary structures.

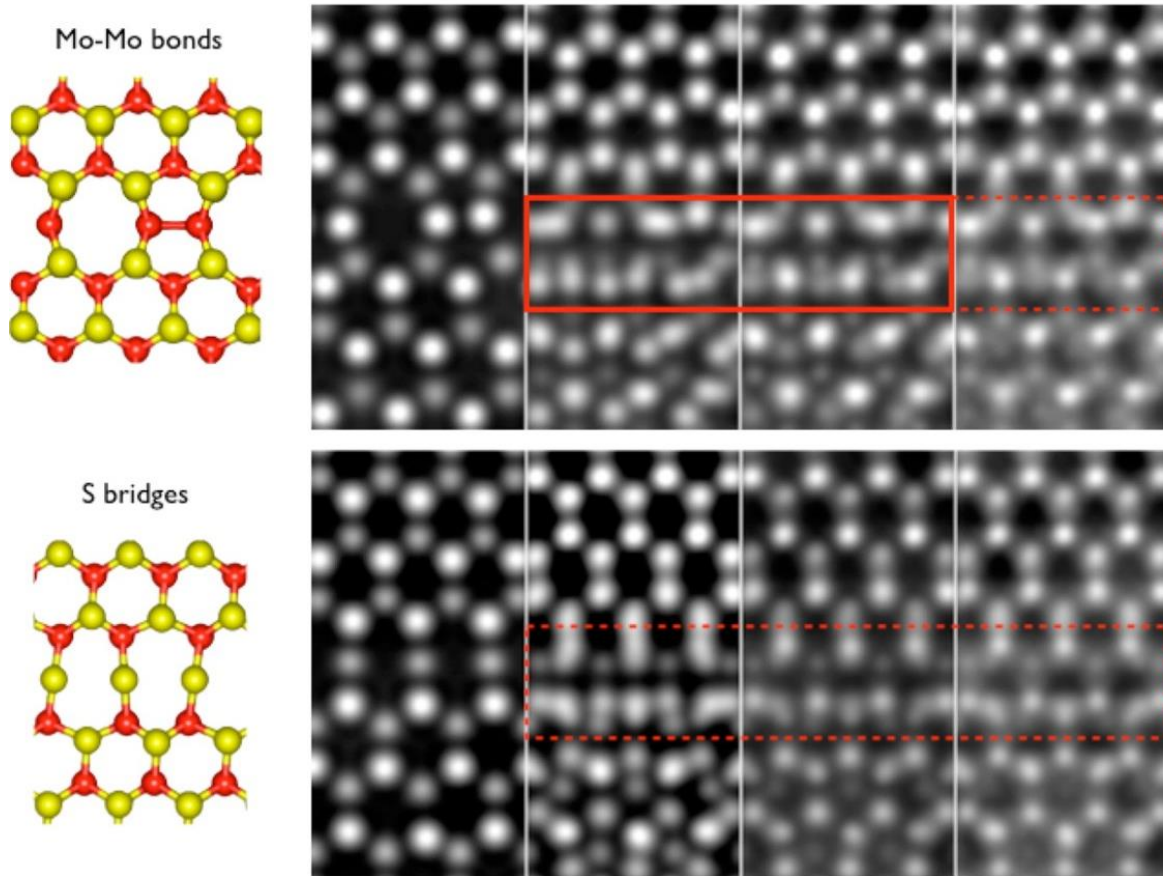


Figure 1.7 60° tilt grain boundary structures of monolayer MoS_2 predicted and observed by Enyashin *et al.* [65].

These previous studies provide useful knowledge about the mechanical properties of MoS_2 such as the in-plane elastic modulus, the breaking forces, the ultimate strain and strength, the role of mechanical strain on thermal conductivity, and the characterization of defects and their effects on electronic properties. However, there are many drawbacks in these studies. (1)

The mechanisms which lead to failure have never been elucidated by the experimental indentation on the monolayer MoS₂ membranes. (2) The impacts of structural defects on the mechanical properties of monolayer MoS₂ still remain unknown due to the restricted length scale of quantum mechanical methods. (3) These methods can only study systems with the number of atoms range from a few up to hundreds. While it is possible study the electronic properties with quantum calculations, it is impossible to extract reasonable mechanical properties and failure mechanisms from these small systems. Therefore, it is essential to use classical atomistic simulations to generate larger systems for the investigation of the mechanical properties of monolayer MoS₂ and how sensitive mechanical properties are to defects.

1.4 Thesis objectives

For this thesis, the two main objectives are (1) to gain insight about the failure mechanism of monolayer MoS₂ by modeling nanoindentation performed on suspended free standing membranes with comparison to experiment and (2) to explore the influence of structural defects on the mechanical properties of monolayer MoS₂ by modelling monolayer MoS₂ membranes with defects and simulating the same nanoindentation process as in part (1).

Chapter 2 will provide an overview of methods and equations used in this research. Chapter 3 will discuss the deformation and failure mechanisms of defect-free monolayer MoS₂ membranes. “Multiaxial tension simulations are performed via nanoindentation on suspended membranes, analogous to experiments presented in the literature [26,51,53]. The force required for fracture is computed for different indenter and membrane diameters and compared directly to experimental results, providing a means to assess the accuracy of the interatomic potential used in this work” [26]. This interatomic potential was developed and parameterized by Liang *et al.* [66,67] to study the frictional behavior of MoS₂ structures. It was modified and employed into

LAMMPS by Stewart and Spearot [35] to investigate defect formation mechanisms of layered MoS₂ under nanoindentation via molecular statics simulations. In Chapter 3, the roles of different parameters such as the operating temperature of the system, the shape of the membrane, and the speed of the indenter on the mechanical properties as well as the failure mechanisms of monolayer MoS₂ are discussed. To explore the deformation and failure mechanisms, several structural analyses on the lattice are performed.

On the other hand, Chapter 4 will focus on the effects of structural defects on the mechanical performance of monolayer MoS₂. Two different types of defects are studied: point defects and grain boundaries. For point defects, monosulfur vacancy is investigated due to its frequent observation in experiment [62,64]. Various combinations of membrane sizes and vacancy densities are employed to study their roles on the mechanical properties. For grain boundaries, different structures reported by experimental characterization or computational prediction [63–65] are generated. The calculated vacancy formation and grain boundary energies are compared with density functional theory calculations [62–65] to ensure the integrity of the interatomic potential in capturing these defects. Similarly to Chapter 3, multiaxial tension simulations are performed via nanoindentation on suspended defect-containing membranes. The direct comparison between mechanical properties of defect-containing membranes with defect-free ones provides insight regarding how structural defects influence the mechanical properties of monolayer MoS₂.

CHAPTER 2: BACKGROUND

2.1 Atomistic simulations

Atomistic simulation is a computational modeling technique used to study the atomic level structure and behavior of materials. There are two main branches of atomistic simulation methods which are quantum mechanical methods and classical atomistic methods. Some typical quantum mechanical methods are density functional theory, pseudopotential theory, and first principle calculations. Each involves various approximations of the solution to electronic Schrödinger equations for atoms and molecules. The quantum mechanical methods are generally accurate since they account for the electronic structure of every atom. However, they are extremely expensive in terms of computational resources limiting their applicability to study systems composed of less than a few hundreds of atoms. On the other hand, classical atomistic methods combine the electrons and nucleus together to model each atom as a sphere with mass, m . This reduces the number of degrees of freedom in the simulation resulting in considerably less computational cost. Therefore, classical atomistic methods can model significantly larger systems up to several millions of atoms allowing the study of [68–73]:

- (a) the time evolution of the system when disturbed by external condition settings such as temperature or pressure. This is extremely useful when studying the structural changes of the system during the phase transitions.
- (b) failure mechanism such as fracture and how different parameters affect its rate and mechanism.
- (c) defects such as free surfaces, grain boundaries, dislocations, and vacancies.

Although experiment can capture and characterize these defects, it is challenging

for experiments to gain insight about the time evolution of these structures: how they initiate and influence the properties of materials.

There are three different techniques in classical atomistic simulations: Monte Carlo, molecular statics, and molecular dynamics simulations. In this thesis, the nanoindentation process is simulated via molecular dynamics simulations while molecular statics is used to find the equilibrium structures of the grain boundaries in Chapter 4. Section 2.2 and 2.3 will briefly discuss the concepts of both of these techniques. Comprehensive discussions about Monte Carlo method as well as quantum mechanical methods can be found in references [68–73].

As mentioned earlier, the atoms are modeled as a point mass without the concept of electrons in classical atomistic simulations. Therefore, these simulations require a special function to characterize the interaction energy among atoms in the system, commonly known as the interatomic potential function, U . The interatomic potential function depends solely on the positions of each individual atom in the system. The forces acting on atom i due to the neighboring atoms is then determined as the negative gradient of this potential function [68–73].

$$\vec{F}_i = - \frac{\partial U}{d \vec{r}_i} \quad \text{Equation 2.1}$$

where \vec{r}_i is the position vector of the i^{th} atom. Section 2.4 will provide more detail about interatomic potentials as well as the specific MoS₂ interatomic potential utilized in this work.

Depending on the complexity of the interatomic potential and the computational resources, atomistic simulations can model up to several millions of atoms. While this system size is much larger than that from quantum mechanical methods, it is tiny compared to the number of atoms in a macro scale system (on the order of 10^{23} [72]). The atoms at the boundaries of the simulation cell have less neighboring atoms, resulting in free surfaces. The common

method to eliminate free surfaces and imitate a bulk environment is to apply a computational trick: periodic boundary conditions [68–73]. Figure 2.1 shows a two dimensional demonstration for a simulation cell containing 4 atoms with periodic boundary conditions.

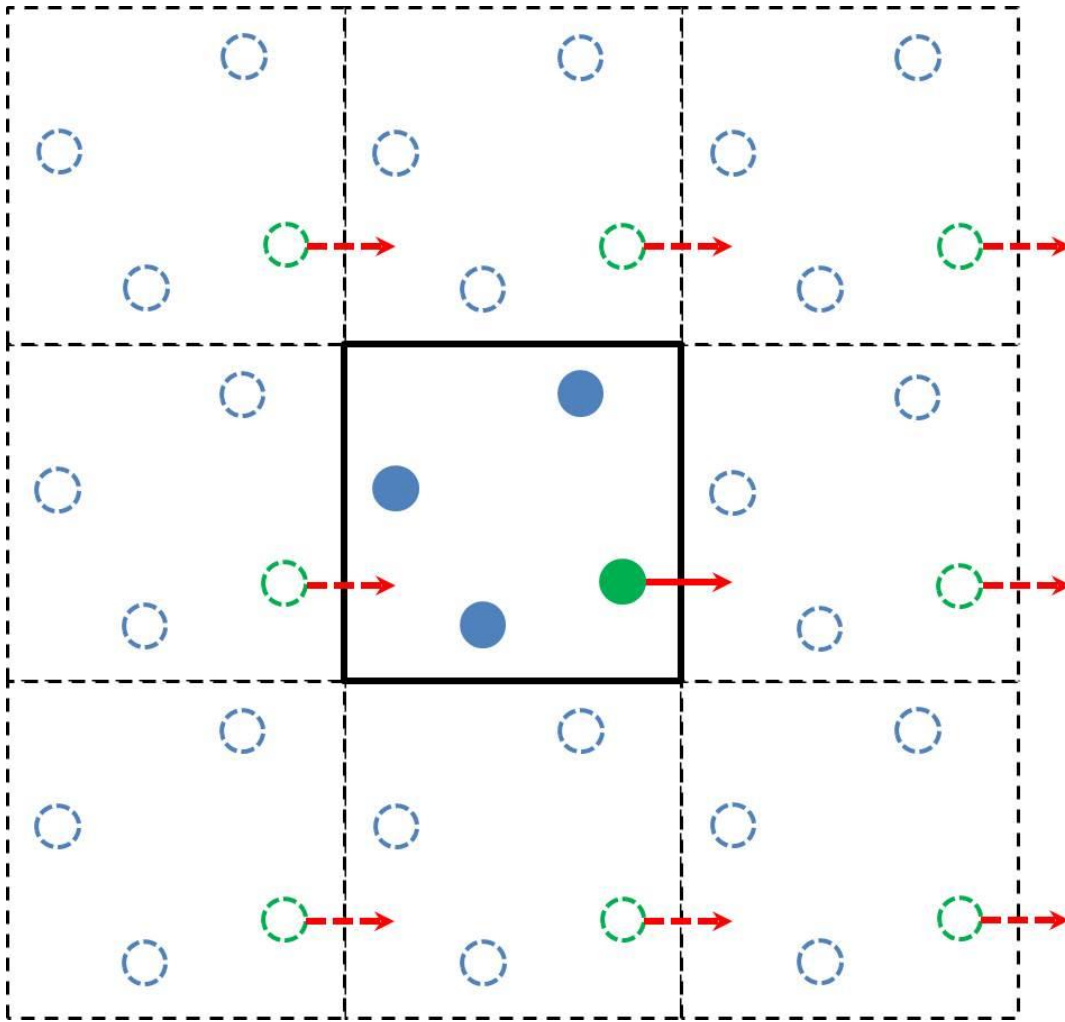


Figure 2.1 Periodic boundary conditions in two dimensions.

The simulation cell containing 4 “real” atoms (shown by solid lines) is surrounded by its replicated images with “ghost” atoms, with identical properties to the “real” atoms (shown by dashed lines). The image cells are continually repeated to produce infinite number of atoms,

replicating the bulk environment. As shown by the red arrows in Figure 2.1, all “ghost” atoms move exactly the same way the “real” atom in the simulation cell moves. If an atom leaves the simulation cell through a boundary, one of its images will enter the simulation cell through the opposite boundary. The atoms that are close to the boundary of the simulation cell can interact with “ghost” atoms in the image cell, eliminating the free surface effect. However, there are two issues that need to be considered when using periodic boundary conditions [68–73]. First, the size of the simulation cell must be at least 2 times larger than the cut-off distance for the interatomic potential to avoid interaction between atoms and their own images. Second, for simulations studying defects in materials, periodic boundary conditions replicate the defect of the simulation cell, increasing the defect density. In order to minimize the effects of these artifacts, the simulation cell size should be carefully chosen. Typically, periodic boundary conditions are extremely useful tool used to study bulk materials. However, it is undesirable to use periodic boundary conditions along the Z axis perpendicular to the basal plane when investigating 2D material properties. In this research, the boundary condition is fixed in all three directions to mimic free standing membrane of monolayer MoS₂.

For our simulations, the classical molecular dynamics code LAMMPS, which is developed and distributed by Sandia National Laboratories, is utilized [74]. The current version of LAMMPS is written in C++ and has a collection of implemented interatomic potentials allowing the modeling of various types of materials and systems. Atomistic simulations performed using LAMMPS provide dump files as an output. The dump files contain all of the information such as atom index number, positions, or velocities of every atom in the system. For this study, potential energy of each atom is outputted as an indication for any irregular mechanism throughout the deformation process. The Open Visualization Tool (OVITO) is then

used to open these dump files, allow visualization of each individual atoms and perform extra calculations such as atom displacements, centrosymmetry parameters, or bond angles from the simulations [75].

2.2 Molecular dynamics simulations

Molecular dynamics simulation is a branch of classical atomistic simulations that studies the time evolution trajectories of a system of particles (atoms, molecules, or united atoms) deterministically by numerically integrating their equations of motions. In this research, the particles are considered as atoms. From the trajectories of all the atoms, the macroscopic collective properties of the system such as temperature, pressure, or potential energy can be extracted using thermodynamic averaging. This section provides a brief overview of molecular dynamics simulation and how it is set up in this research via LAMMPS. A more comprehensive review of molecular dynamics simulation, its advantages, limitations, and applications can be found in references [68–73].

Given a system of N atoms, the goal of molecular dynamics simulations is to solve the classical equations of motion for this N -body system:

$$\begin{aligned}\dot{r}_i &= \frac{p_i}{m_i} \\ \dot{p}_i &= F_i\end{aligned}\tag{Equation 2.2}$$

where r_i , p_i , m_i is the position, momentum, mass of atom i , respectively. F_i is the total force acting on atom i due to interacting with neighboring atoms or an external force. This system of coupled ordinary differential equations, however, is insufficient to capture and simulate various scenarios of experiments since it does not couple with temperature or pressure boundary

conditions. Indeed, Equation 2.2 is only used for isolated systems where the number of atoms and the shape, volume, and energy of the simulation cell remain constant during the time integration, known as the microcanonical ensemble (NVE). Some other common used ensembles are the canonical ensemble (NVT) and the Gibbs ensemble (NPT). In the NVT ensemble, the volume of the simulation cell is fixed, but heat is exchanged with the environment through the cell boundaries. On the other hand, the NPT ensemble allows the isotropic or anisotropic modification of the dimensions of the simulation cell under external work or pressure. For extended system with more complex settings, the generalized system of coupled ordinary differential equations [76,77] are

$$\begin{aligned}
 \dot{r}_i &= \frac{p_i}{m_i} + \eta(r_i - R_o) \\
 \dot{p}_i &= F_i - (\eta + \xi I)p_i \\
 \dot{\xi} &= v_T^2 \left(\frac{T}{T_o} - 1 \right) \\
 \dot{\eta} &= \frac{v_p^2}{NkT_o} V(P - P_o) \\
 \dot{h} &= \eta h
 \end{aligned}
 \tag{Equation 2.3}$$

, where η and ξ are the frictional parameters to couple atoms to a desired pressure and temperature bath, v_T and v_p are damping coefficients to modify the rate of convergence to a desired temperature and pressure, R_o is the center of mass of the system, V_o and P_o are the desired temperature and pressure, and k is the Boltzmann's constant. The first 2 equations are the modified versions of the classical equations of motion, while the 3 new equations adjust the atom velocities and simulation cell shape according to the external temperature and pressure.

Despite the extra complexity to Equation 2.3 compared to Equation 2.2, the method of solving them is identical. There are three required components of the molecular dynamics

simulation technique. First, the force acting on every atom via the neighboring atom interactions must be known given the trajectories of each atom. As shown earlier, this is done using the interatomic potential, which will be discussed in Section 2.4. Second, an efficient algorithm is required to accurately solve this N -body system of coupled first order ordinary differential equations. There are several methods for numerically integrating the equations of motion such as 4th order Runge-Kutta method, Verlet algorithm, leapfrog iteration method, or velocity Verlet algorithm. The velocity Verlet algorithm is the most efficient algorithm with balanced accurate result,

$$\begin{cases} r_i(t + \Delta t) = r_i(t) + \Delta t v_i(t) + \frac{1}{2} (\Delta t)^2 a_i(t) \\ v_i(t + \Delta t) = v_i(t) + \frac{1}{2} \Delta t [a_i(t) + a_i(t + \Delta t)] \end{cases} \quad \text{Equation 2.4}$$

where v_i , a_i are the velocity, acceleration of atom i , which corresponding to the momentum and force. Velocity Verlet algorithm, the only one incorporated in LAMMPS for molecular dynamics simulation, is dominant since it requires only 1 force calculation per time iteration, and the error term is proportional to the square of the time increment. Unlike Verlet algorithm and leapfrog algorithm, velocity Verlet can output the velocities of every atom at the current time step without any supplemental post-processing. Third, as for any numerical integration methods, the initial conditions including the positions and velocities of every atom are required. Typically, the initial atom positions are defined on a lattice with primitive and basis vectors. Random values for initial velocities of atoms in the simulation are desired [72,73]. The net of these velocities must be shifted to zero and the average of these randomly initial velocities must be scaled consistently with the initial desired temperature of the system. The relationship between temperature and the atom velocities are given as,

$$T = \frac{1}{gkN} \sum_i^N m_i v_i^2 \quad \text{Equation 2.5}$$

where g is the dimension of the system. With these three components, the trajectories of all atoms in the system can be solved from the equations of motion of every atom. While the atom trajectories provide information about how the system evolves at atomic level, they are not very useful when validating the results of the simulation. To compare results from molecular dynamics simulations with experimental values, it is necessary to derive the macroscopic properties of the system from the time evolution of atomic positions and velocities using statistical mechanics. For instance, the macroscopic temperature of the system is the time average of instantaneous temperature values computed by Equation 2.5. Therefore, it is extremely important to understand how certain properties oscillate to average over a proper time period.

2.3 Molecular statics

Molecular statics is another branch of classical atomistic simulations that studies the relaxed configuration of atoms deterministically in a zero temperature system. The equilibrium structure of atoms is found by minimizing the potential energy of the system [78]. There are several energy minimization methods such as conjugate gradient, steepest descent, and Newton-Raphson. In this thesis, conjugate gradient and steepest descent are utilized to relax the defect-containing membranes generated in Chapter 4. The rest of this section provides an overview of both of these methods. More detailed discussion about the mathematical expressions and how to implement them into a computer algorithm can be found in Schewchuk [78].

Graphically, energy minimization is the the process of searching for the configuration of atoms (x) from initial configuration (x_0) that minimizes the potential energy function, $U(x)$. There are two major components of this searching process that differentiate between energy minimization methods. The first component is the direction of the search, d , and the second component is where to stop searching along that direction and look for a new direction. The first component, direction of the search, is the main difference between conjugate gradient and steepest descent methods. However, the search direction at the first step of both methods is identical. From calculus, the gradient always points toward the direction of steepest increase of that function. Therefore, the negative of the gradient points in the direction that steepest decrease of that function. For atomistic simulations, the negative of the gradient of the potential energy, $U(x)$, is the force vector, F . Thus, the position after the first searching step can be expressed as,

$$x_{(1)} = x_{(0)} + \alpha f_{(0)} \quad \text{Equation 2.6}$$

where $x_{(0)}, x_{(1)}$ are the configuration at step 0 and 1, $f_{(0)}$ is the force unit vector at step 0, α is the distance travel along the force vector direction, which is the second component. In both methods, α is chosen to minimize the potential energy along the force vector direction via a line search algorithm. There are 3 different line search methods incorporated in LAMMPS: backtrack, quadratic, and force zero, which the backtrack line search algorithm set as default. The result of choosing α that way is the orthogonality of the previous search direction with the gradient direction of the next step. For steepest descent method, the search direction is always defined as the force vector direction. As a result shown in Figure 2.2, their successive search directions are always orthogonal, which potentially leads to slow convergence for ill-conditioned

systems. To avoid the repetition in the search direction, new search directions are constructed in a way that they are conjugate with previous search direction,

$$d_{(m+1)} = f_{(m)} + \beta_{(m+1)} d_{(m)} \quad \text{Equation 2.7}$$

where β is the parameter to ensure the conjugate among all of the search directions. For nonlinear conjugate gradient method, there are 3 well known ways to compute β : Fletcher-Reeves, Polak-Ribiere, and Hestenes-Stiefel. The Polak-Ribiere formula has a faster rate of convergence [79] and is the method incorporated in LAMMPS:

$$\beta_{m+1}^{PR} = \frac{f_{m+1}^T (f_{m+1} - f_m)}{f_m^T f_m} \quad \text{Equation 2.8}$$

However, the Polak-Ribiere could cycle infinitely in some cases [78]. Typically, when $\beta_{m+1}^{PR} < 0$, the conjugate gradient method is restarted with the first direction search using the steepest descent.

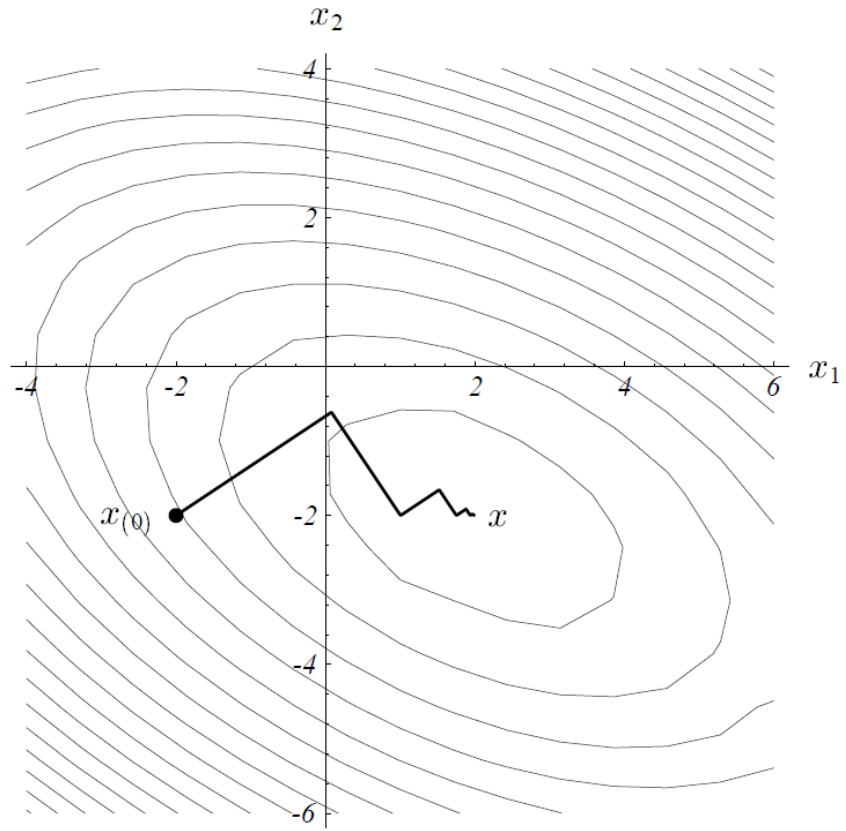


Figure 2.2 Graphical illustration of steepest descent method [78].

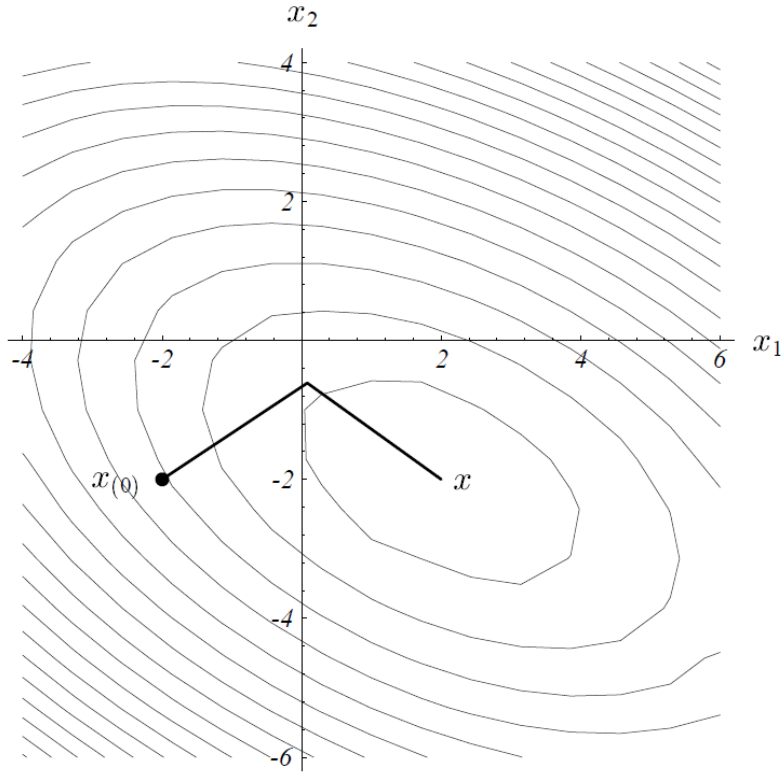


Figure 2.3 Graphical illustration of conjugate gradient method [78].

2.4 Interatomic potential

2.4.1 Introduction

As defined in Section 2.2, classical atomistic simulations model the electrons and nucleus as a point mass. As a result, they employ the idea of a special function, known as an interatomic potential, to compute the potential energy associated with interatomic interactions given the atom positions. The accuracy of the interatomic potential significantly influences the result of the simulations. Therefore, it is crucial to choose an appropriate interatomic potential depending on different parameters of the atomistic simulations. Typically, the focus when choosing the interatomic potential is the type of material to model and the process to simulate. There is no common form for an interatomic potential. Typically, there are two different

approaches for choosing the form of an interatomic potential: analytical form from quantum mechanical concepts or pure mathematical cubic spline. The parameters are then fitted and adjusted to the database of experimental data depending on the application of the interatomic potential.

Based on the level of complexity, an interatomic potential can be categorized into 4 classes: pair potentials, cluster potentials, pair functionals, and cluster functionals [79]. In the simplest class, the pair potentials describe the atomic interaction depending solely on the distance between 2 atoms. They assume that the bond strength is independent of the bond angles between triplet atoms and the environment. On the other end of extremely complex, the cluster functions could incorporate both 3-body or 4-body terms in the local coordination to calculate the interaction among atoms. A more comprehensive review of interatomic potential can be found in Calrsson [79]. Section 2.4.2 discusses briefly the interatomic potential for monolayer MoS₂ used in this research.

2.4.2 MoS₂ interatomic potential

This project employs the MoS₂ interatomic potential, which was parameterized and implemented into LAMMPS by Stewart and Spearot [35]. It combines the many-body reactive empirical bond-order (REBO) potential and the two-body Lennard-Jones (LJ) potential [66,67]. While the REBO portion can capture the covalent bond breaking and creation, the LJ portion can represent the non-bonded van der Waals interactions between layers or atoms far apart within the same layer. The equation for the reactive empirical bond order potential given by Liang *et al.* [66] is expressed as,

$$\begin{aligned}
E_{REBO} &= \frac{1}{2} \sum_{i \neq j} f_{ij}^c(r_{ij}) [V^R(r_{ij}) - b_{ij} V^A(r_{ij})] \\
&= \frac{1}{2} \sum_{i \neq j} f_{ij}^c(r_{ij}) \left[\left(1 + \frac{Q_{ij}}{r_{ij}} \right) A_{ij} e^{-\alpha_{ij} r_{ij}} - b_{ij} B_{ij} e^{-\beta_{ij} r_{ij}} \right]
\end{aligned} \tag{Equation 2.9}$$

where r_{ij} is the distance of separation between atoms i and j , $f_{ij}^c(r_{ij})$ is the cutoff function, $V^R(r_{ij})$ and $V^A(r_{ij})$ are the pair potential terms that only depend on the distance between atoms to represent the repulsive and attractive interactions, respectively, and b_{ij} is the many-body bond order function that modifies atomic interactions according to environment such as local coordination or angles between triplet of atoms. On the other hand, the LJ portion is a common 12-6 potential given by the following equation:

$$E_{LJ} = 4\varepsilon_{ij} \left[\left(\frac{\sigma_{ij}}{r_{ij}} \right)^{12} - \left(\frac{\sigma_{ij}}{r_{ij}} \right)^6 \right] \tag{Equation 2.10}$$

where ε_{ij} and σ_{ij} are LJ parameters for different pairs of atoms. The repulsive interaction part is modeled by $(\sigma_{ij}/r_{ij})^{12}$, while the attractive interaction part is represented by $(\sigma_{ij}/r_{ij})^6$. The attractive term is dominant at large distance; however, as atoms get closer, the repulsive term is more influential to avoid atoms overlapping with each other. Most importantly, combining both of them, this REBO style interatomic potential can reproduce the DFT calculations of the crystal properties such as bond length, bond stiffness, and the c_{33} elastic constant of MoS₂ by Alexiev *et al.* [80]. Especially, the accuracy of the c_{33} elastic constant, which is defined as the stiffness along the c axis perpendicular to the basal plane, is very essential for this study since

nanoindentation along the *c* axis is simulated. Detailed descriptions about the parameters for REBO and LJ part of this Mo-S potential can be found in Stewart and Spearot [35].

2.5 Atomistic simulations of nanoindentation

As discussed in Chapter 1, nanoindentation on a suspended free standing membrane is a very common experimental technique used to study the mechanical behavior of thin film structures under multiaxial tension [13,50,51,53]. For 2D materials with typical thickness less than 10 nm, it is very difficult, maybe even impossible with the current technology, to apply uniaxial tension by gripping and stretching the sheet of material. By measuring the force on the indenter and tracking its positions, experimentalist can generate the force displacement curve for the nanoindentation process [81,82]. Not only mechanical properties such as hardness and elastic modulus of the thin film structure but also nanoscale behaviors such as phase transformations can be derived from this curve [82].

However, experimental nanoindentation is incapable of explaining the mechanism of these properties and behaviors [83]. With a rapid increase in computational power, atomistic simulations can now model very large systems comparable to experimental sizes. Therefore, atomistics simulation of nanoindentation can gain insights regarding how atomic behaviors such as defect nucleation, phase transformation, or dislocation motion correspond to experimentally measureable properties [83–85]. There are still, however, some limitations with atomistic simulations of nanoindentation such as the speed of the indenter and the size of the simulation. Due to the restricted time scale, the speed of the indenter in atomistic simulations is at least 3 orders of magnitude larger than experimental nanoindentation [83]. Moreover, it is still

contemporarily demanding to model 2D membranes with experimental sizes via atomistic simulations.

There are 2 common methods to model the indenter in atomistic simulations of nanoindentation. The indenter can be physically generated as a group of atoms or imaginarily modeled as a frictionless sphere with an expression to characterize the force exerted on the atoms. For this research, the indenter is modeled as an ideal frictionless spherical indenter where there is only repulsive force between the indenter and atoms [74,86]. This repulsive force is defined as:

$$F(r) = -K (r_i - R)^2 \quad \text{Equation 2.11}$$

Here, K is the force constant, R is the radius of the indenter, and r is the distance from atom i to the center of the indenter [74,86]. If the indenter does not interact with the atoms, indicated by $r_i \geq R$, the force in Equation 2.11 is set to zero. On the other hand, if $r_i < R$, indicating that the indenter are in contact with atom i , there will be a repulsive force computed by Equation 2.11 acting on atom i .

CHAPTER 3: SIMULATION AND CHARACTERIZATION OF NANOINDENTATION ON PERFECT 2D MEMBRANE

In this chapter, the focus is to simulate experimental nanoindentation on suspended free standing membranes of monolayer MoS₂ without any structural defects. There are 3 objectives of this chapter. First, by comparing the breaking forces from our simulations with experimental results, the accuracy of the REBO style interatomic potential is assessed and validated. Second, the roles of several parameters such as the shape of the membrane, the sizes of the indenter and membrane, the temperature, and the indenter speed on the mechanical performance of monolayer MoS₂ are discussed in Section 3.2. Finally, failure mechanism of monolayer MoS₂ is captured and described in Section 3.3.

3.1 Simulation methodology

To mimic experimental nanoindentation on free standing membranes, circular membranes of monolayer MoS₂ with fixed boundary conditions are generated. “The boundary of the membrane is rigidly clamped with a thickness of approximately 1 nm” [26]. With this configuration, the force acting on the boundary atoms in each direction is set to zero during the simulations, which are marked by the black outer circle in Figure 3.1a. As a result, the boundary atoms are stationary during the indentation process. The top view of the circular membrane in Figure 3.1b shows that the S and Mo atoms are in hexagonal structure (shown by the green and black hexagons respectively). On the other hand, Figure 3.1c shows that the membrane only composed of 1 S-Mo-S trilayer.

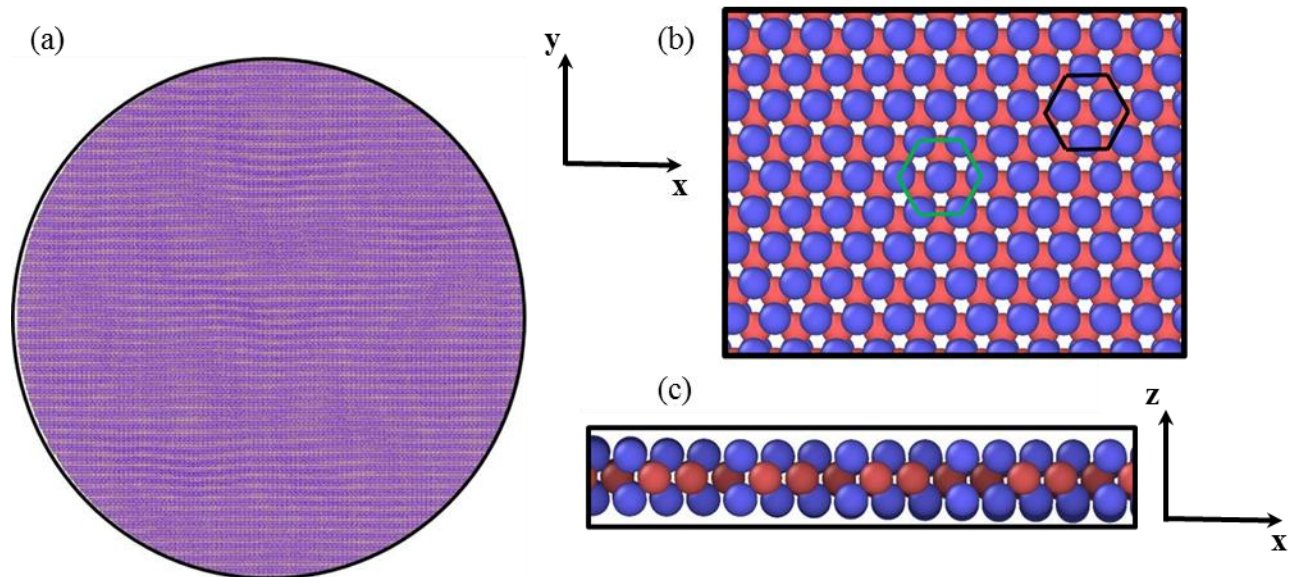


Figure 3.1 Monolayer MoS₂ membrane with fixed boundary condition to mimic experimental settings. Blue atoms are S, red atoms are Mo. a) Top view. b) Top view zoom-in. c) Side view zoom-in

To study the role of size on the mechanical properties and failure mechanism of monolayer MoS₂, different combinations of membrane and indenter diameters are studied. In this work, membrane diameters of 100, 150, 200 and 250 nm and indenter diameters of 20, 30, 40 nm are selected. These ranges of values are chosen in an effort to closely replicate experimental conditions. The indenter diameters in this study are in the range of experimental nanoindenter sizes, which are from 10 to 50 nm [51,53]. However, the common membrane diameter for experimental nanoindentation is 500 nm [51,53] which is double the largest membrane used in these simulations. The main reason for this gap is because of the size of the simulation for larger membranes. The number of atoms is proportional to the surface area, which is proportional to the squared of the radius. As shown in Table 3.1, the number of atoms is quadruple when double the membrane diameter from 100 to 200 nm. Larger membranes increase not only the number of

computations for each time step but also the number of time steps required to observe failure. Therefore, double the size of the membrane expands the computational complexity by approximately 16 times.

Table 3.1 Number of atoms in monolayer MoS₂ circular membrane at different membrane diameters

Membrane Diameter (nm)	100	150	200	250
Number of Atoms	278,583	626,763	1,114,314	1,741,296

“To generate a state of multiaxial tension, nanoindentation is performed on a suspended circular monolayer of MoS₂ with the basal plane of the MoS₂ lattice parallel to the XY plane and perpendicular to the Z direction. Before the nanoindentation process, the system is equilibrated to 10 K for a period of 100 ps to minimize thermal vibration using the Nosé – Hoover thermostat” [77]. Commonly, the temperature for MD simulation is room temperature 300 K to mimic the environment condition of the experimental works. For our research, the temperature is set to 10 K to minimize the thermal vibrations of atoms in order to identify the structural deformations due to tension. The simulations are run under the canonical ensemble, commonly known as NVT ensemble, which maintains constant number of atoms, system volume, and system temperature with a variable pressure. “Nanoindentation is performed at the center of each membrane using a spherical indenter which exerts a repulsive force on atoms in the monolayer” [26]. Here, the force constant is taken as 10 eV/Å³ [35,86,87]. “The indenter speed is specified as 10 m/s, which is fast compared to experiment; however, as discussed earlier, it is reasonable relative to prior MD simulations” [26,83]. Supplemental simulations of nanoindentation on the 200 nm-diameter membrane with the same 20 nm-diameter indenter at different indenter speeds of 10, 7.5, and 5 m/s are performed to investigate the effects of the indenter speed on the

mechanical properties as well as the failure mechanism of monolayer MoS₂. Force-displacement curves are obtained and compared with those from experiments [51,53].

3.2 Force-displacement curve

“Force-displacement curves are generated for every nanoindentation simulation performed on the suspended MoS₂ monolayer sheets. The force on the indenter is calculated as the sum of atomic forces acting on the indenter, while displacement is computed as the average Z direction displacement of the atoms in a 1 nm radius region at the center of the membrane. Breaking force is defined as the maximum force acting on the indenter during the indentation. To avoid inappropriate size effects, only simulations that have a ratio between membrane and indenter diameter greater than or equal to 5 are considered in the results” [26].

3.2.1 Role of membrane shape

“Figure 3.2 shows typical force-displacement curves for models in which the membrane diameter is more than 5 times larger than the indenter diameter. As shown in Figure 3.2, the relationship between applied force and deflection is only linear for small forces (less than 10 nN). At larger applied force, this relationship becomes nonlinear, which is consistent with experimental observations [51,53]. For the circular membrane, there are two points of interest in Figure 3.2: A minor and a major drop force at about 260 and 320 Å, respectively. A stress-induced displacive phase transformation, which is “the rearrangement of atomic lattice structure to accommodate relatively large amounts of inelastic deformation,” [88] beneath the indenter is observed immediately preceding the major force drop, which ultimately results in the fracture of the membrane. The structural and visual analysis of this phase transformation related to the major force drop will be discussed in Section 3.3. To explore the source of the minor force drop, supplemental MD simulations are performed using a square membrane. There is a slight shift of where failure occurs which could be explained by the difference between the areas of the square and circular membranes for the same radius. As shown in Figure 3.2, these simulations show only the major force drop implying that the minor force drop is an artifact of the clamped circular geometry. Most importantly, it is found that the breaking force is not influenced by the geometry of the MoS₂ membrane nor is the observation of the phase transformation” [26].

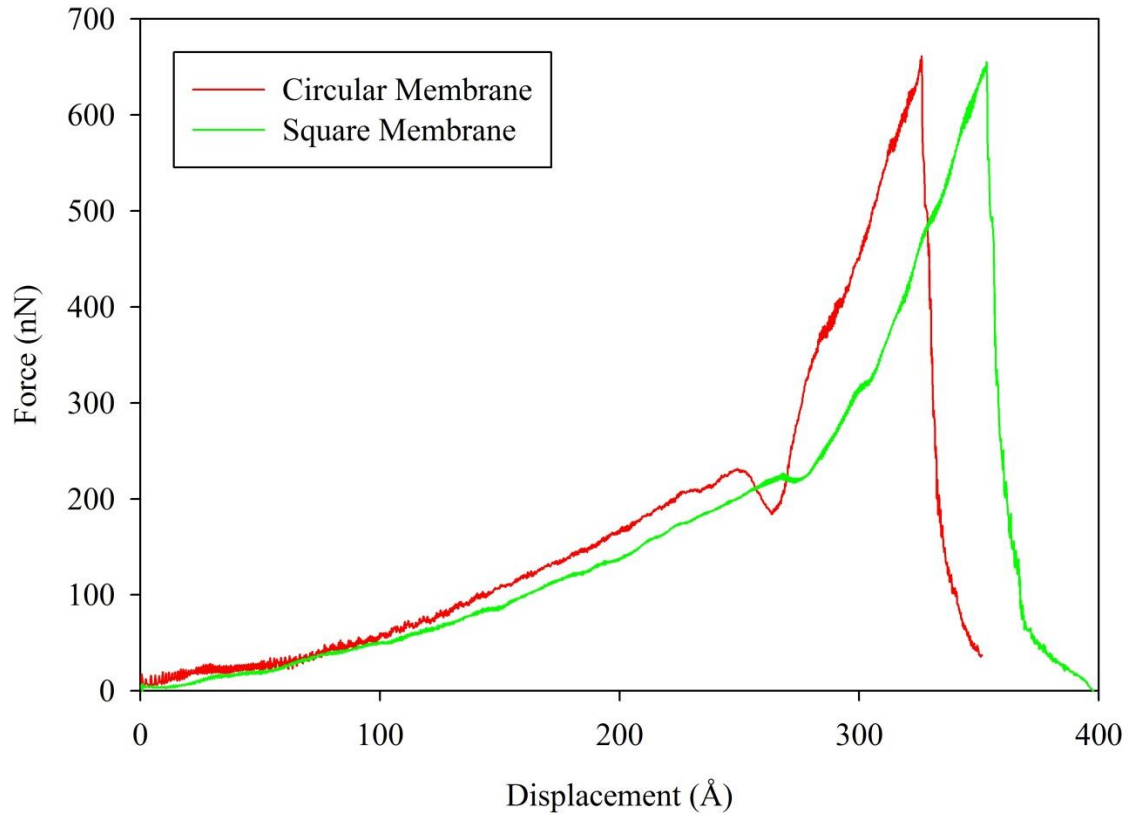


Figure 3.2 A typical force – displacement curve for nanoindentation on suspended circular monolayer MoS₂ sheets with a diameter of 200 nm and an indenter diameter of 40 nm [26].

3.2.2 Role of indenter and membrane sizes

As mentioned earlier, one of the objectives of this work is to investigate the role of membrane and indenter sizes on the breaking force and failure mechanism of monolayer MoS₂ by employing different combinations of indenter and membrane diameters. Breaking force magnitudes of all simulations are reported in Table 1. There is a similar phase transformation observed in all simulations which proves that indenter and membrane sizes have no effect on the failure mechanism of monolayer MoS₂.

Table 3.2 Breaking forces for each simulation in this work. Breaking forces are reported in nN and indenter and membrane diameters are reported in nm [26].

Indenter \ Membrane	100 nm	150 nm	200 nm	250 nm
20	324	330	329	321
30	541	489	491	490
40	994	711	661	662

From Table 3.2, it is recognized that for simulations that have a ratio between membrane and indenter diameter less than 5, there is a significant increase in the required breaking force. Because the membrane is relatively small in this case, there are possible effects from boundary atoms that were fixed during the indentation, which raises the effective stiffness of the membrane. As a result, these relatively small membrane scenarios have higher breaking forces. Also, for experimental works, the lowest ratio between membrane and indenter diameter is about 10 [51,53]. Therefore, for our analysis, only simulations that have ratio between membrane and indenter diameter greater than or equal to 5 are considered.

“To assess the accuracy of the REBO style interatomic potential, the force required for fracture for each combination of membrane and indenter diameter is compared to that reported by experiments in the literature. Figure 3.3 shows the breaking force versus nanoindenter diameter for each simulation performed in this work and two experimental values for monolayer MoS₂ fracture from the literature [51,53]. The breaking forces from our simulation are in the reasonable range of experimental values. Also, as the indenter diameter increases, the force necessary to break the membrane also increases. This observation is consistent between both simulation and experiment. For example, Cooper *et al.* [53] reported an average breaking force of 1500 nN with standard deviation of 300 nN using the tip of an atomic force microscope (AFM) to perform nanoindentation on multiple free-standing monolayers of MoS₂. The diameter of their circular membranes was 500 nm, while the diameter of their AFM tip was 52 nm. Bertolazzi *et al.* [51] performed a similar experiment on a suspended circular MoS₂ membrane with a diameter of 550 nm and an indenter diameter 24 nm and reported an average breaking force of 200 nN. The molecular dynamics simulations in this work using a REBO style interatomic potential provide breaking forces in reasonable agreement with those reported in the literature. For small indenters, the breaking forces from our simulations seem to overshoot due to the perfect crystal structures in the simulated membranes. For larger indenters, deviation between experiment

and simulation breaking forces could be due to slippage that occurs at the clamped boundary of the monolayer of MoS₂ in experiments during nanoindentation (shown recently for graphene [89]) or limitations of the REBO style interatomic potential to model large deformations in monolayer MoS₂” [26].

To study the role of membrane size, force-displacement curves for simulations with the same indenter diameter and different membrane diameters are compared. Figure 3.4 shows the force-displacement curves for various sizes of suspended sheets with the indenter diameter of 20 nm. There are some subtle differences between these curves such as the displacement points where failure occurs and the positions of the minor force drop, which are possibly due to the effect of fixed boundary on the circular membrane. However, the breaking forces of all of these simulations are relatively close. This result shows that the multiaxial tension stress state is localized at the center region of the membrane; as a result, the breaking force is independent of the membrane diameter.

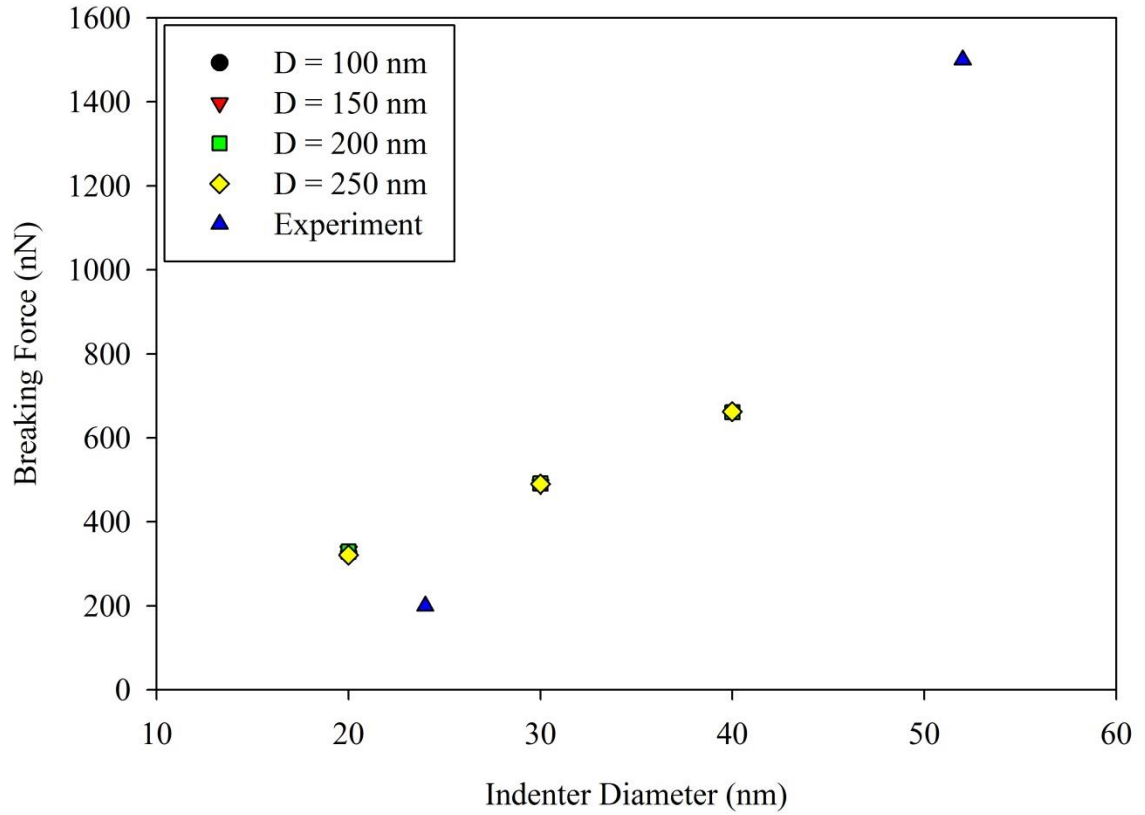


Figure 3.3 Breaking force as a function of indenter diameter for nanoindentation on suspended circular single layer MoS₂ sheets with different membrane diameters. Data from simulations that have a ratio between membrane and indenter diameter less than 5 are not included [26].

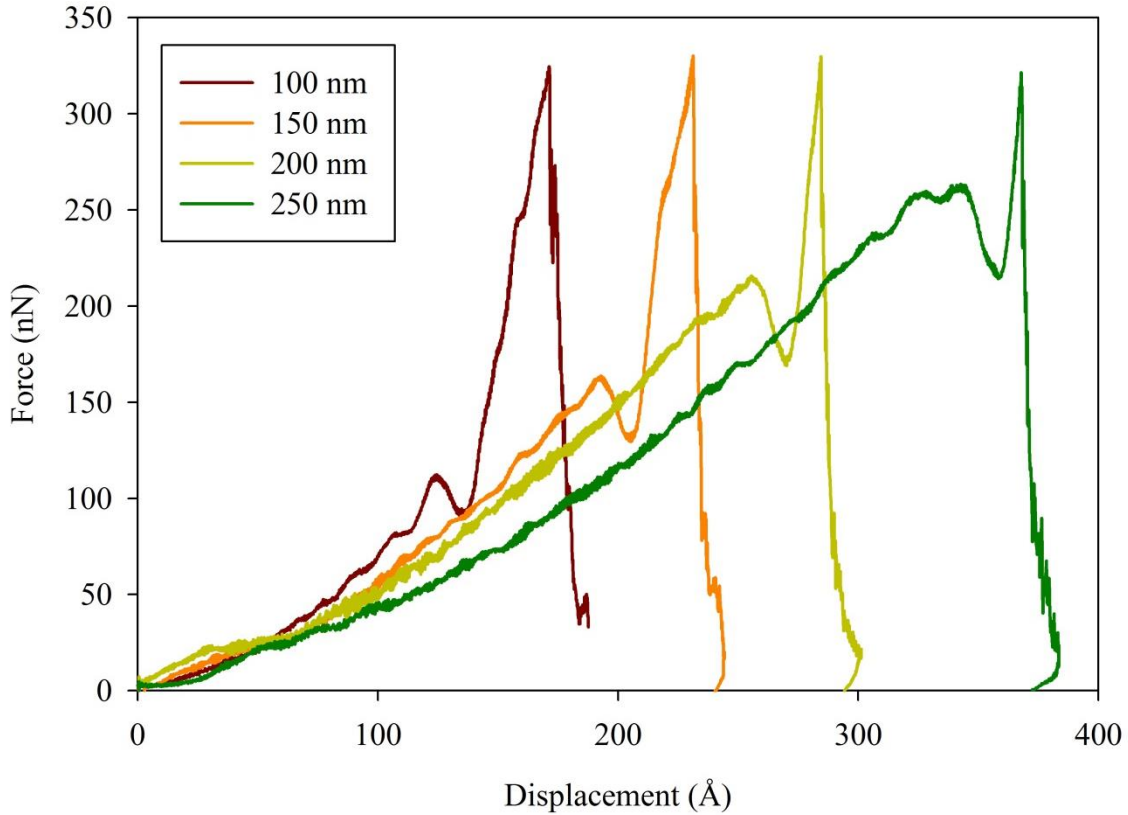


Figure 3.4 Force – displacement curve for nanoindentation on suspended circular monolayer MoS₂ sheets with an indenter diameter of 40 nm and different membrane diameters.

3.2.3 Role of indenter speed

As mentioned earlier, the MD indenter speed of our simulations is fast compared to experimental work. To study if the observed deformation and failure mechanisms are sensitive to the indenter speed, MD simulations of monolayer MoS₂ under slower indenter rates are performed. The force-displacement curves for these simulations with membrane and indenter diameter of 200 and 20 nm are plotted in Figure 3.5. It shows that while they have different curve shapes, their breaking force magnitudes are relatively close. Also, the phase transformation is observed for slower indenter speed simulations. Thus, the breaking force and the phase transformation observed in this study are independent of the indenter speed within the range studied.

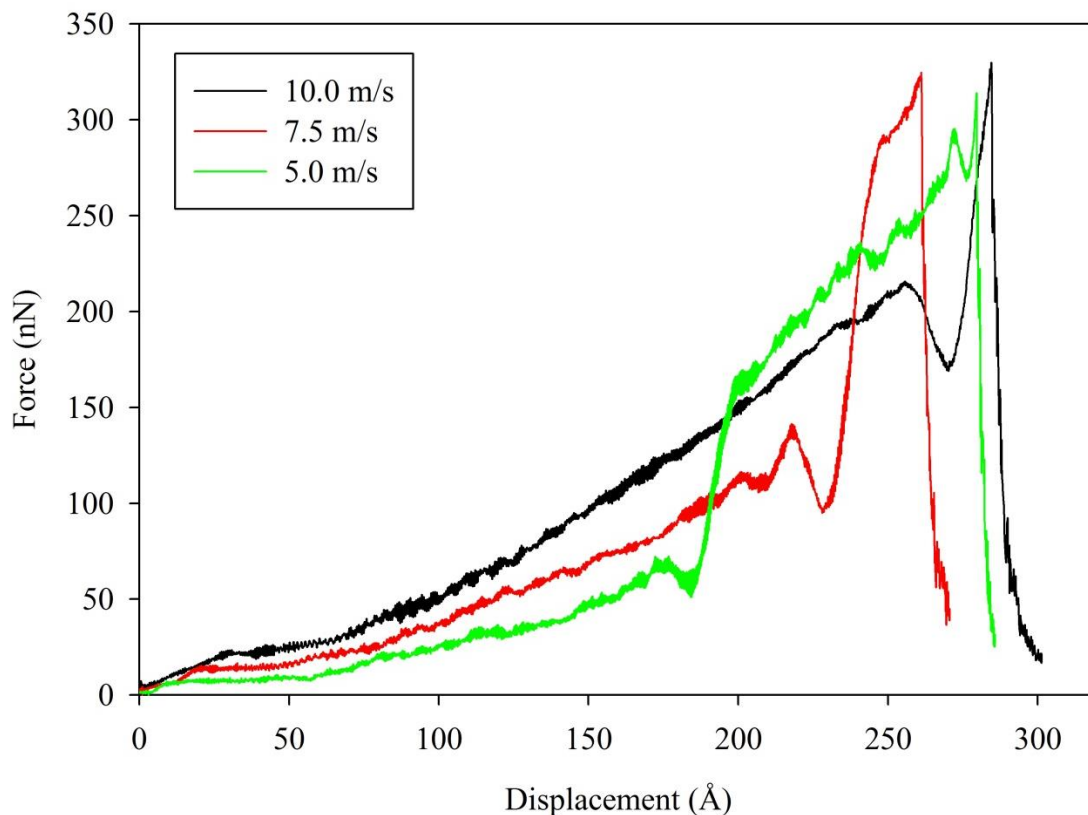


Figure 3.5 Force – displacement curve for nanoindentation on suspended circular monolayer MoS₂ sheets with a diameter of 200 nm and an indenter diameter of 20 nm at different indenter speed.

3.3 Phase transformation

In the last section, the accuracy of the Mo-S system interatomic potential used in our study is assessed by comparing the breaking forces with those in experiment. Ultimately, the main objective is to use this interatomic potential to explore the failure mechanism of monolayer MoS₂, which could not be done by experimental works. To explore the failure mechanism a visual analysis is performed via potential energy of the S atoms. As shown in Figure 3.6, there is a new phase distinct from the original phase.

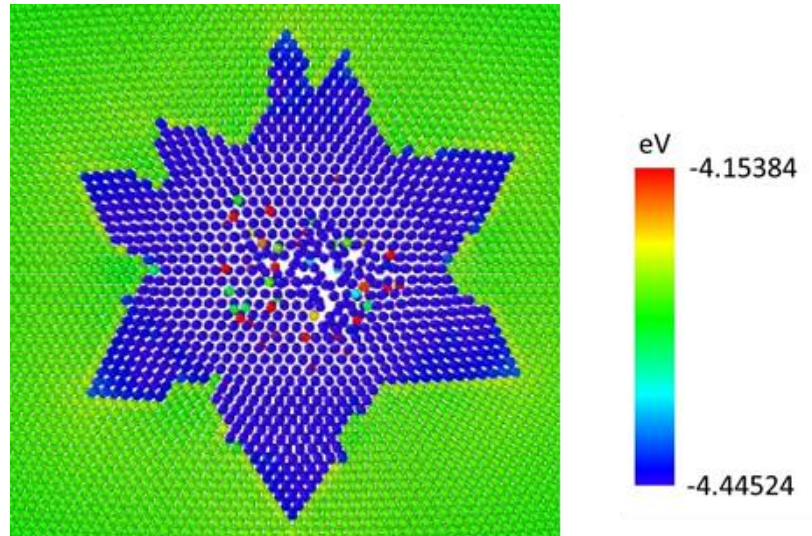


Figure 3.6 Top view of the phase transformation colored by S potential energy (the membrane and indenter diameters are 150 and 40 nm, respectively). Atoms colored blue have undergone the phase transformation [26].

The same phase transformation is observed when removing S atoms and coloring Mo atoms by potential energy. Obviously, the system has gone through a phase transformation resulting in this new phase with different structure and potential energy level. The next objective of this study is to discover the structure of this new phase. Since monolayer MoS₂ shares many similarities with graphene such as hexagonal lattice structure, 2D materials, and potential replacement for Si, a first possible deformation mechanism is lattice distortion within each hexagonal S or Mo layer similar to the Stone – Wales defects found in graphene [90]. To explore this in-plane deformation, the dimensions of the hexagonal lattice units are measured in both new and original MoS₂ phases. Then, these lattice units are directly compared to capture any displacements or rotations of the atoms. The detail of this direct comparison method can be found in Joseph Simpson’s Undergraduate Honor Thesis [91]. As shown in Figure 3.7, results confirm that the new MoS₂ phase, even though it stretches uniformly, remains hexagonal.

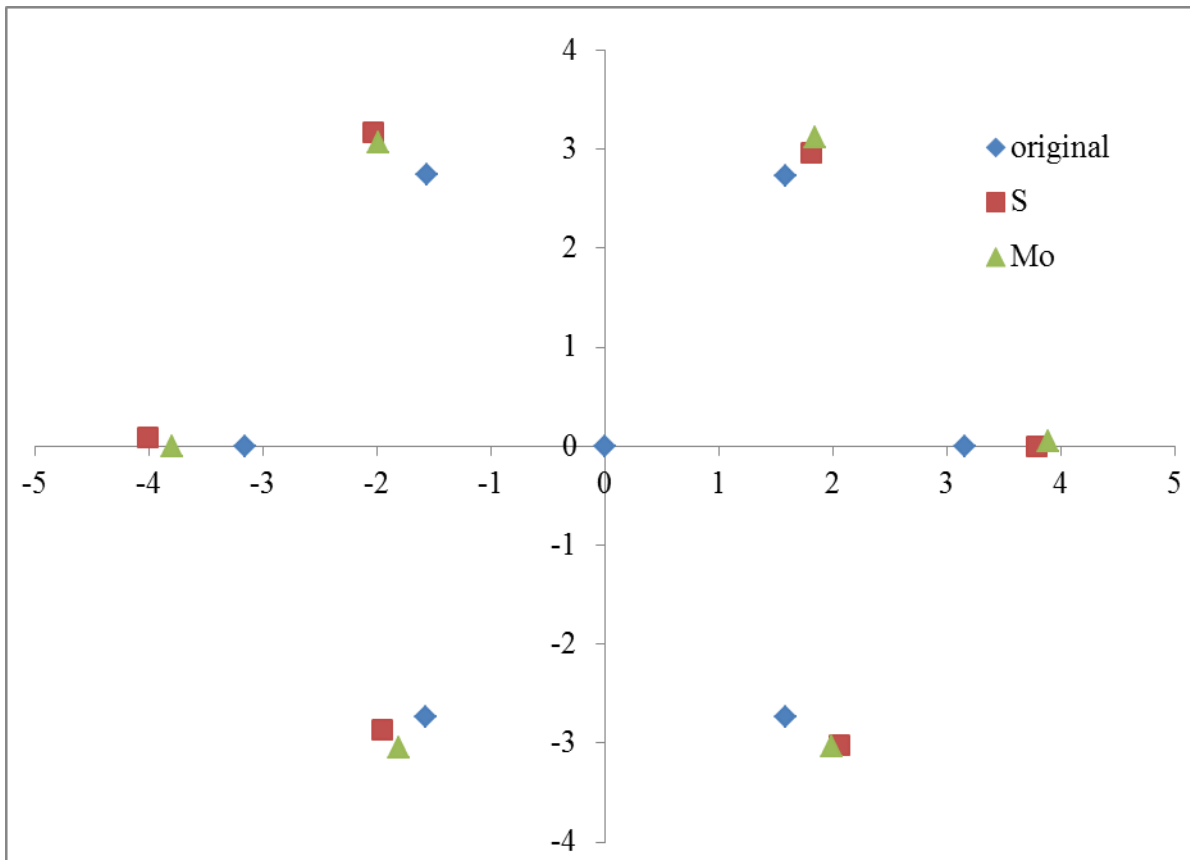


Figure 3.7 Hexagonal lattice units of Mo, S in the new phase compared to original structure

Unlike graphene, which is only composed of 1 layer of carbon atoms, monolayer MoS₂ is composed of a S-Mo-S trilayer. Therefore, the phase transformation could be a result of an intralayer structural change. To investigate if this intralayer structural deformation is the source of the phase transformation, visual analysis is performed via potential energy of both Mo and S atoms.

“Figure 3.8 captures the point of initiation of the new phase in monolayer MoS₂ sheets with a membrane diameter of 200 nm. The phase transformation starts with a change in the potential energy of 2 S and 4 Mo atoms, without any apparent change in the hexagonal crystal structure. When comparing the positions and angles these 6 new phase atoms with the surrounding original phase atoms, the S-S intralayer Z dimension distance of the new phase S pair is significantly shorter than those of surrounding S pairs. Therefore, it is hypothesized that this

new phase involves a change in the S-S intralayer Z dimension distance which influences the S-Mo-S angles within the monolayer of MoS₂” [26].

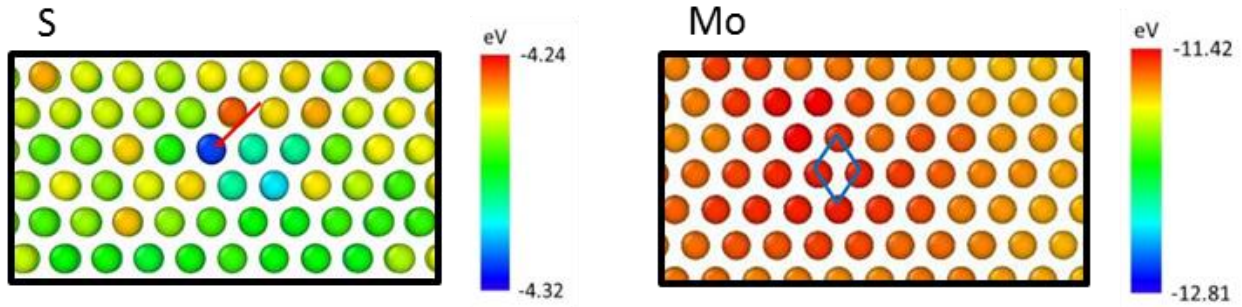


Figure 3.8 Top view of the phase transformation initiation. In the left figure, Mo atoms are removed, coloring S atoms by potential energy; a pair of S atoms is marked by the red arrow. In the right figure, S atoms are removed, coloring Mo atoms by potential energy; the corresponding 4 Mo atoms are marked by the blue rhombus [26].

To confirm that the phase transformation is indeed caused by the S-S intralayer Z dimension distance drop, the intralayer distance between S atoms versus time step for simulations with different membrane sizes using a 40 nm diameter indenter was plotted in Figure 3.9. An abrupt drop from 3.1 Å to 2.9 Å is observed at the time step associated with the phase transformation in each membrane. Once nucleated, the new phase propagates outward from the region beneath the indenter, as shown in Figure 3.6.

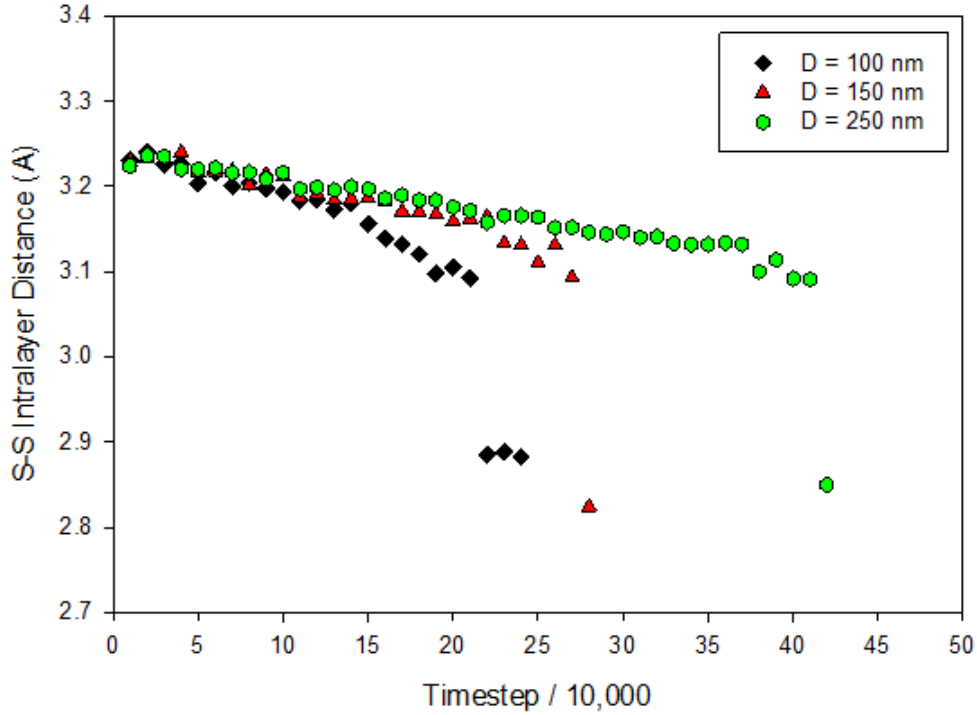


Figure 3.9 S-S intralayer distance versus simulation time step for different membrane diameters using the same indenter diameter of 40 nm [26].

“A similar phase transformation is found during uniaxial tension in the zigzag direction (which is along the X axis) at 300K prior to fracture of the MoS₂ monolayer [26,91], which demonstrates that the observed deformation and failure mechanisms in this work are independent of the tension state and temperature. This supplemental simulation is studied by Joseph Simpson as part of his Undergraduate Honor Thesis [91]. Figure 3.11 shows a visual analysis by atomic potential energy showing the propagation of the phase transformation in a MoS₂ monolayer at a strain of 11.5%. Identical to the multiaxial tension analysis, the structure of the phase transformed region is analyzed by measuring the shape and size of the hexagonal lattice units. Unlike the multiaxial tension simulations, there is a slight distortion of the hexagonal lattice structure during uniaxial tension in the zigzag direction. This is apparent in Figure 3.11 as a shift of one atomic layer occurs across the new phase. Figure 3.10 shows that the hexagonal lattice units are sheared by the phase transformation with atoms displaced by an average magnitude of 0.48 Å. Similar to the multiaxial deformation simulations, for uniaxial tension in the zig-zag direction, it is found that the S-S intralayer distance abruptly decreases (original phase is 3.21 Å while this distance is 3.15 Å for the phase transformed region). The calculated Young’s modulus for uniaxial tension in the zig-zag direction is 232 GPa, which is in reasonable agreement with DFT calculations of 187 [92] and 220 GPa [46]. Also, the stress corresponding to the phase transformation is 20.6 GPa while the ultimate strength from DFT calculations are 16.9 [92] and 19.3 GPa [46]. A possibly similar phase

transformation with no distortion of the 2H hexagonal structure was reported for bulk MoS₂ under compression at 20.5 GPa using a diamond anvil test [93]; no evidence of phase transformations has been reported previously in monolayer MoS₂. Ultimately, bond breaking occurs beneath the indenter leading to a crack at the center of the membrane” [26].

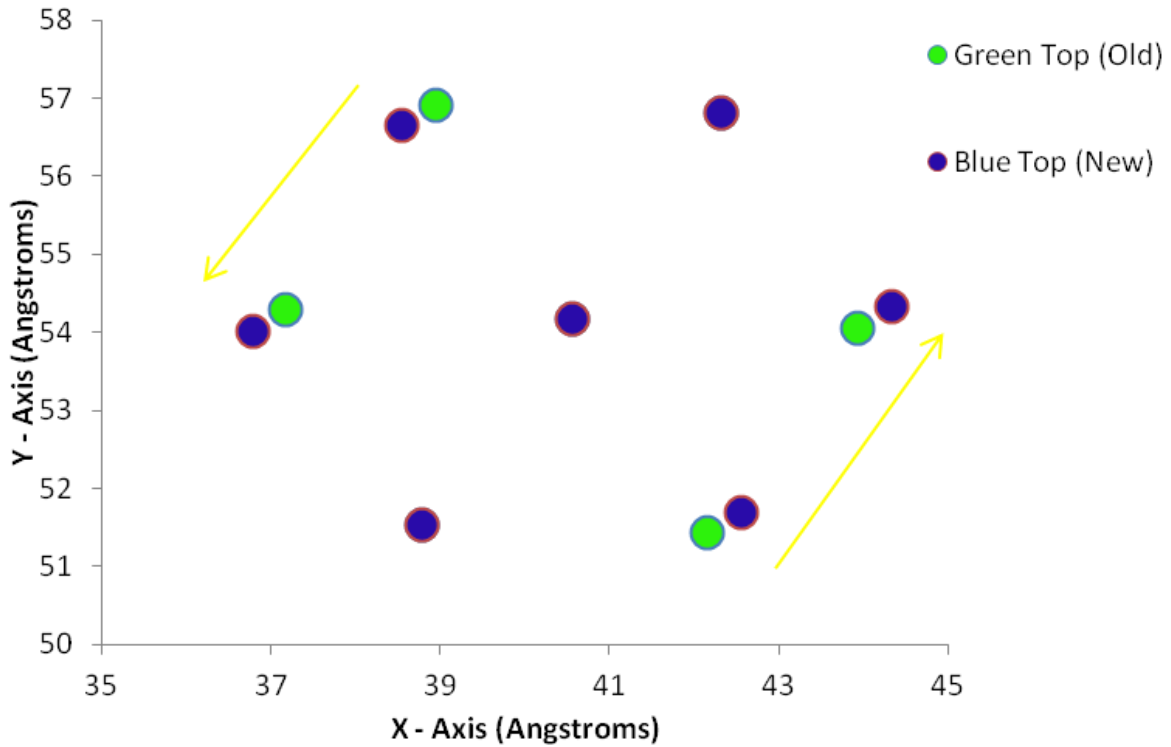


Figure 3.10 Comparison of the hexagonal lattice units between original and new phases indicating the magnitude and the direction of the shear distortion [26,91].

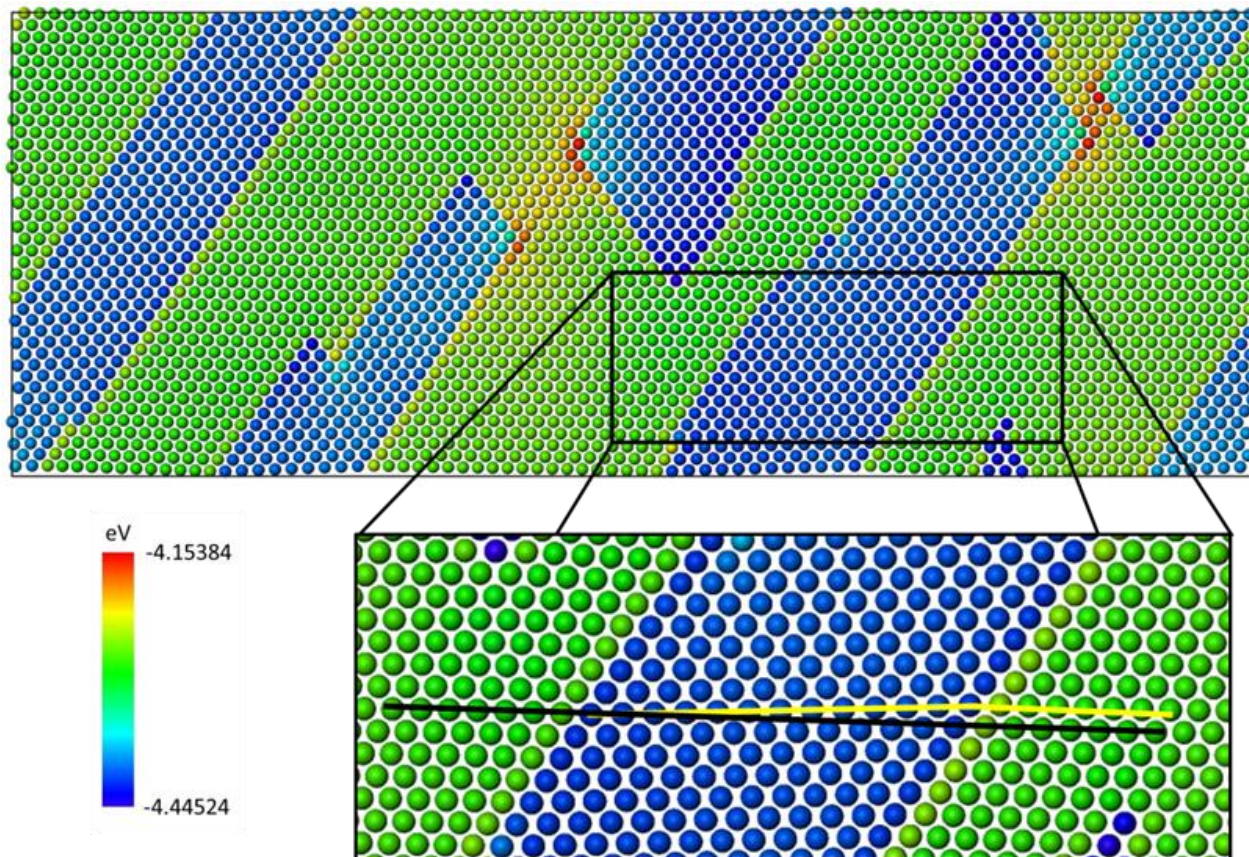


Figure 3.11 Propagation of the phase transformation during uniaxial tension. The expanded view allows for visual analysis as a black line is drawn between the original phases (green) across the new phase (blue) illustrating the distortion of the lattice in the zig-zag direction [26,91].

CHAPTER 4. SIMULATION AND CHARACTERIZATION OF NANOINDENTATION ON FREESTANDING MoS_2 MEMBRANES WITH DEFECTS

In this chapter, structural defects are introduced into the monolayer MoS_2 membrane to study their role on the mechanical properties and failure mechanisms observed in Chapter 3. Two types of defects are considered in this research: point defects and grain boundaries. Point defects are commonly observed in 2D materials, particularly monolayer MoS_2 , due to the imperfection of the growth process [57,94]. Experimentally, it was identified that there are 6 common types of point defects in CVD grown monolayer MoS_2 [64]. As shown in Figure 4.1, they are monosulfur vacancy (V_S), disulfur vacancy (V_{S_2}), vacancy complex of Mo and nearby three sulfur (V_{MoS_3}), vacancy complex of Mo nearby three disulfur pairs (V_{MoS_6}), and antisite defects where a Mo atom substituting a pair of S atoms (Mo_{S_2}) or a pair of S atoms substitute a Mo atom ($S_{2\text{Mo}}$). Monosulfur vacancy, which is an absent of a S atom, is the most common point defect structure, repeatedly observed in experimental samples because it has the lowest formation energy. It was shown theoretically and experimentally that it is unlikely for these monosulfur vacancies to combine and form disulfur vacancy [64], which is a missing of a pair of S atoms that overlapped when observed from the top view (along the Z direction). Recently, it was shown computationally and experimentally that monosulfur vacancies can be introduced into the monolayer membrane via electron irradiation [62]. It was also proved that monosulfur vacancy in the bottom layer of the membrane is more likely to happen under deformation. For this research, monolayer MoS_2 membranes with monosulfur vacancies in the bottom layer of the membrane are investigated to understand the role of point defect on the mechanical performance of monolayer MoS_2 .

On the other hand, grain boundary structures and their influence on the electronic properties for both low (about 20°) and high (60°) tilt angles of synthesized monolayer MoS_2 have been characterized and studied. Depending on the tilt angles and the relative position between 2 grains, there could be different type of grain boundary structures such as 5- and 7-fold rings [64], 8-4-4 rings [57], or 4-fold-coordination S atoms instead of regular 3-fold-

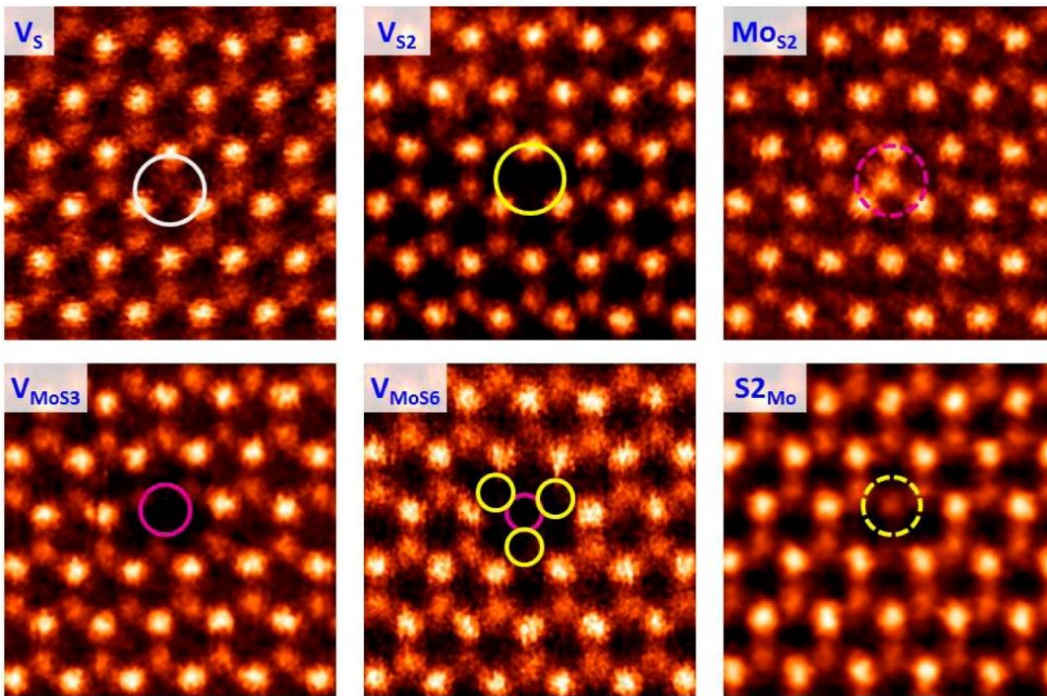


Figure 4.1 Different point defects in monolayer MoS_2 observed via scanning transmission electron microscopy by Zhou *et al.* [64].

coordination ones [63,64]. Unlike graphene which restores its perfect crystal structure under 60° symmetric tilt due to the hexagonal crystal structures, there are several 60° symmetric tilt grain boundary structures predicted [63] and observed experimentally [64] for monolayer MoS_2 . For this research, the goal is to predict all the possible structures of monolayer MoS_2 60° symmetric

tilt grain boundaries and their influence on the mechanical properties via atomistic simulations. Section 4.1 presents the simulation methods used to generate structural defects and deform the defect-containing monolayer MoS₂ membranes. Section 4.2 compares the computed potential energies of these defects to DFT calculations from literature. The influences of monosulfur vacancy and its density on the mechanical performance are also discussed. Finally, Section 4.3 shows different structures of symmetric 60° tilt grain boundary and how they affect the mechanical behaviors of monolayer MoS₂.

4.1 Simulation method

4.1.1 Point defects

Before introducing point defects into the monolayer MoS₂ membranes, it is essential to ensure the ability of the REBO style interatomic potential to model the vacancy in the bottom S plane. Supplemental simulations are performed where circular monolayer MoS₂ membranes are generated with single S vacancy at the center of the bottom layer of the membrane. The systems are then equilibrated using energy minimization method implemented in the LAMMPS package. The energies of the system with and without the defect are recorded to calculate the vacancy formation energy. Vacancy formation energy, usually denoted E_f , is the amount of energy required to create a vacancy. In this research, the vacancy formation energy is defined as,

$$E_f = E_{vac} - (E_{bulk} - \mu_s) \quad \text{Equation 4.1}$$

where E_{vac} and E_{bulk} are still the potential energies of the system with and without a vacancy. μ_s is the chemical potential of S, which is the difference in internal energy of the system when adding 1 atom to the system through the isochoric and isentropic process (constant volume and

entropy) [95]. More detail about how to compute the chemical potential of S is can be found in the review paper about the atomic and electronic structure of MoS₂ particles of Bollinger *et al.* [96]. In this study, the upper and lower bound for the chemical potential are 0 and -1.4 eV, respectively [63,64].

Circular membranes of monolayer MoS₂ with fixed boundary conditions are generated similarly to Chapter 3. To generate monosulfur vacancies of the monolayer MoS₂ membrane, S atoms in the bottom layer are then removed randomly in accordance with a defined ratio within a specified central region [74]. Since the multiaxial stress state is localized at the center, the removal area is specified as a circular central region whose diameter is equal to the diameter of the indenter, which is 20 nm in this study as shown in Figure 4.2.

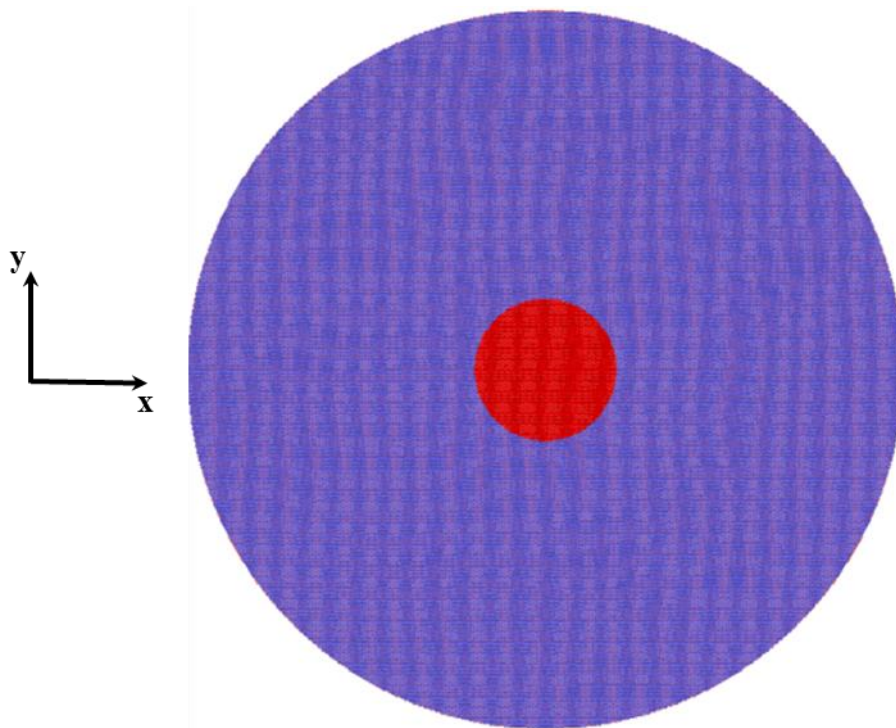


Figure 4.2 Top view of monolayer MoS₂ free standing membrane with membrane diameter of 100 nm. The central red circle is the removal area whose diameter is 20 nm.

With the same input fraction, there is no guarantee LAMMPS would remove exactly the same number of atoms or atoms at the same position for different simulations. To ensure the

validity of the comparisons, simulations with relatively similar number of vacancies are used when investigating the role of membrane size and point defect ratio on the mechanical performance of monolayer MoS₂. Also, to study how the distributions of these vacancies affect the mechanical properties and failure mechanism of monolayer MoS₂, three supplemental simulations with the same membrane diameter of 100 nm and point defect fraction of 0.05 are performed. Various point defect fractions of 0.01, 0.05, and 0.1 are selected to study how vacancy density influences the mechanical performance of monolayer MoS₂.

4.1.2 Grain boundary structures

60° symmetric tilt grain boundary structures are constructed via the following algorithm. First, the membrane is divided along the armchair (Y axis) or zigzag (X axis) into 2 grains where each grain rotates 30° in the opposite direction. Then, the origin is moved by a fraction of the lattice spacing in each dimension; thus, shift and translate the building unit cell of the one grain relative to the other to generate different terminating planes and distances between them at the interface between 2 grains. There are 10 possible moves for each direction X and Y of each grain, resulting in 10,000 possible initial configurations. Finally, after deleting overlapped atoms the system is relaxed via energy minimization and grain boundary energies are recorded. The process is repeated for all the possibilities and pick the representative structure of those with similar grain boundary energies and compare to theoretical studies [63]. Grain boundary energy, denoted as G , is the difference in potential energy between the grain boundary structures with defect-free structures. It is commonly used to identify possible grain boundary structures for different materials. Typically, grain boundary structures with low grain boundary energies are expected to be more stable. For this research, the grain boundary energy is calculated by:

$$G = \frac{E_{GB} - n_{Mo}E_{Mo} - n_S E_S}{L} \quad \text{Equation 4.2}$$

where n_{Mo} and n_S are the numbers of Mo and S atoms in the grain boundary region, E_{Mo} and E_S are the potential energies of single Mo and S atom in defect-free monolayer MoS₂, E_{GB} is the total potential energy of the grain boundary region, and L is the length of the grain boundary region. Here, G is normalized by the length of the grain boundary since the ratio between the thickness of the membrane is negligible compared to the diameter.

With these defect-containing membranes, “nanoindentation is performed via MD simulations along the Z direction, perpendicular to the basal plane of the MoS₂ lattice” [26]. For this research, the effect of structural defects on the mechanical behaviors of monolayer MoS₂ is investigated for different membrane diameters of 100, 150, and 200 nm. “Before the nanoindentation process, the system is equilibrated to 10 K via Nosé – Hoover thermostat” [26,77]. The force constant is 10 eV/Å³ [35,86,87], while the indenter speed is specified as 10 m/s. After the simulations, force-displacement curves are obtained to compare the breaking forces between simulations. Similar to Chapter 3, the force on the indenter is calculated as the sum of atomic forces acting on the indenter, while displacement is computed as the average Z direction displacement of the atoms in a 1 nm radius region at the center of the membrane. Breaking force is defined as the maximum force acting on the indenter during the indentation.

4.2 Effect of monosulfur vacancy on mechanical behaviors of monolayer MoS₂

As shown in Table 4.1, the ranges of values for E_f for single monosulfur vacancy are consistent for different membrane diameters. The ranges of values are also in reasonable agreement with the vacancy formation energy about 6.6 eV for a relaxed single monosulfur

vacancy structure from DFT calculation of Komsa *et al.* [62]. This shows that the interatomic potential used in this research is capable of predicting the point defect formation.

Table 4.1 The vacancy formation energy ranges for monosulfur vacancy using chemical potential ranges of [-1.4,0] eV [63,64] for different membrane sizes. The membrane diameter is in nm.

The vacancy formation energy is in eV.

μ_s \ D _{membrane}	10	60	100	150	200
-1.4 eV	6.475	6.429	6.429	6.667	5.491
0 eV	7.875	7.829	7.829	8.067	6.891

Figure 4.3 shows a typical membrane with monosulfur vacancies generated for this study. The central 20 nm-diameter bottom S layer region contains 3636 S atoms, which also are the 3636 possibilities for monosulfur vacancies. Using the same point defect fraction of 0.05 for 3 differently arbitrary seed numbers, the point defects membranes have slightly different number of monosulfur vacancies with random locations as shown in Table 4.2. The breaking forces from Table 4.2 show that the distribution of the vacancies slightly influences the mechanical properties of monolayer MoS₂. Even though the 1st membrane has the most number of vacancies among the 3, the required force to break this membrane is surprisingly larger than the other 2 membranes. Force-displacement curves from these 3 simulations, plotted in Figure 4.4, are very similar, which shows that small variations in the number of vacancies and their distributions play a minor role in membrane failure.

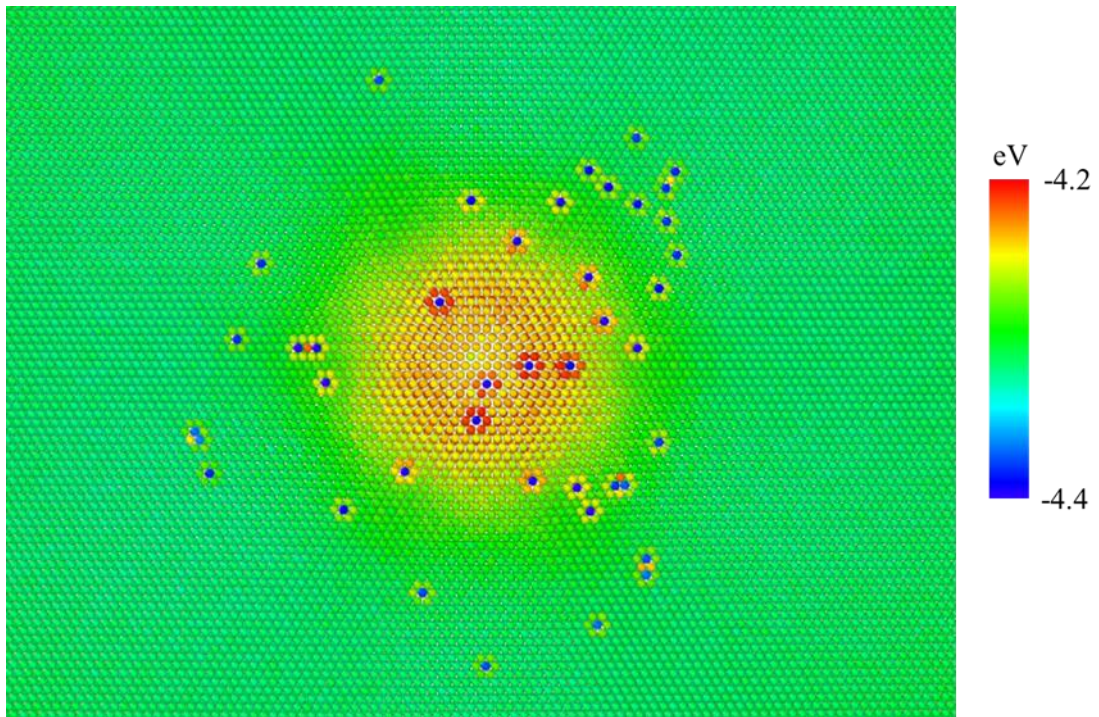


Figure 4.3 Top view of the membrane with monosulfur vacancies colored by S potential energy during the nanoindentation (the membrane and point defect ratios are 100 nm and 0.01, respectively). Atoms colored blue are the top S sulfur atom above a sulfur vacancy.

Table 4.2 Number of vacancies and breaking forces for membranes with the same diameters of 100 nm and different random delete seeds.

run	# of deleted atoms	breaking force (nN)
1	180	295
2	176	287
3	177	291

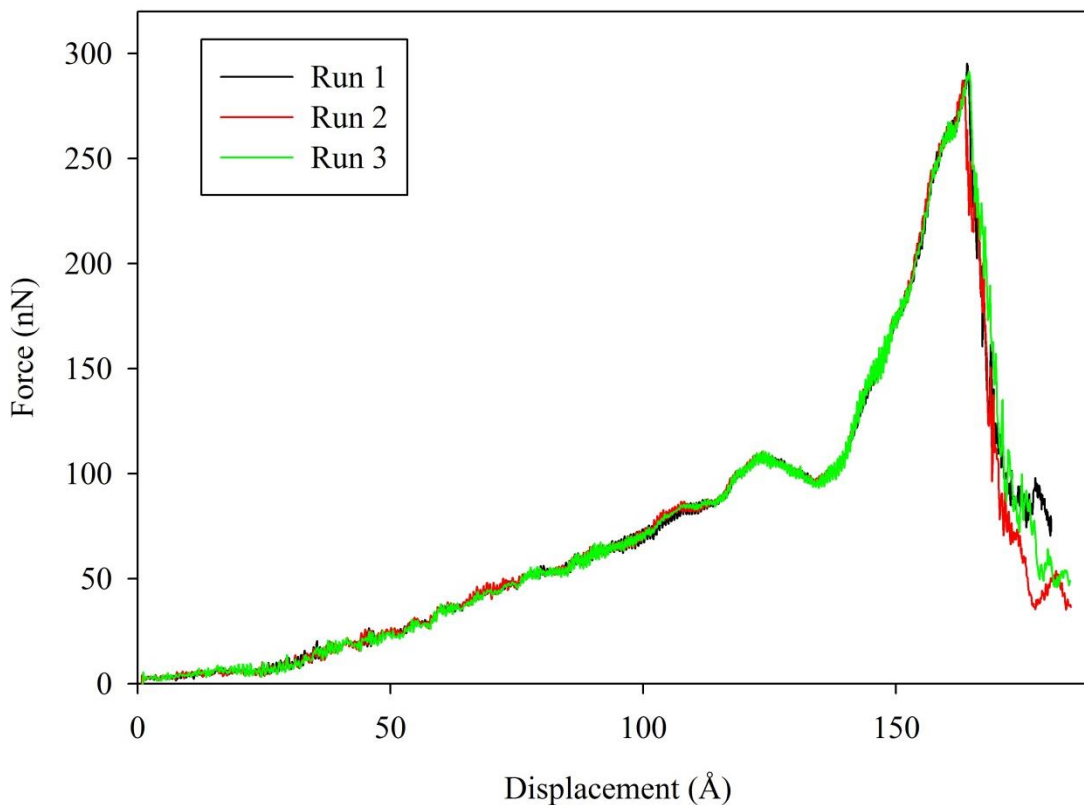


Figure 4.4 Force – displacement curve for nanoindentation on suspended circular monolayer MoS₂ sheets with a diameter of 100 nm and point defect ratio of 0.05 with different random delete seeds.

Breaking force magnitudes of all simulations with different point defect ratios and membrane sizes are reported in Table 4.3. There is a consistent drop in the required breaking force of monolayer MoS₂ membranes with vacancies compared to defect-free membranes in Chapter 3. It is hypothesized that the presence of the monosulfur vacancies modifies the failure mechanism and weakens the mechanical performance of the monolayer MoS₂ membrane. Visual analysis shows that there is still a phase transformation associated with an abrupt drop in S-S intralayer Z dimension distance. However, the phase transformation is not necessarily initiated at the center of the membrane but instead at the accumulated vacancy areas closest to the center as shown in Figure 4.5. Also, from Table 4.3, it is recognized that the breaking force required for

fracture decreases as the point defect ratio increases. As the number of vacancies increases, there is high probability to form regions of accumulated vacancies, promoting stress-concentration points. Therefore, it is possible for the phase transformation to initiate from clusters of vacancies as shown in Figure 4.6, accelerating the new phase propagation process. As a result, membranes with higher number of vacancies fail at lower breaking force. Moreover, simulations of membranes with large number of vacancies show a consistent drop in the breaking force as the membrane size increases. The number of vacancies for all of the membrane sizes is relatively similar since the defined removal region is the same. However, the deformation in the large membrane diameter is more localized. As shown in Figure 4.7, for large membrane diameters, the curves of defect-containing membranes are shifted to the right relative to the curve of the defect-free membrane. This implies that for the same indenting force, membranes with vacancies are under larger displacement at the center compared to the defect-free membrane. This localized deformation results in larger local stresses and thus a lower required breaking force for larger membrane diameters.

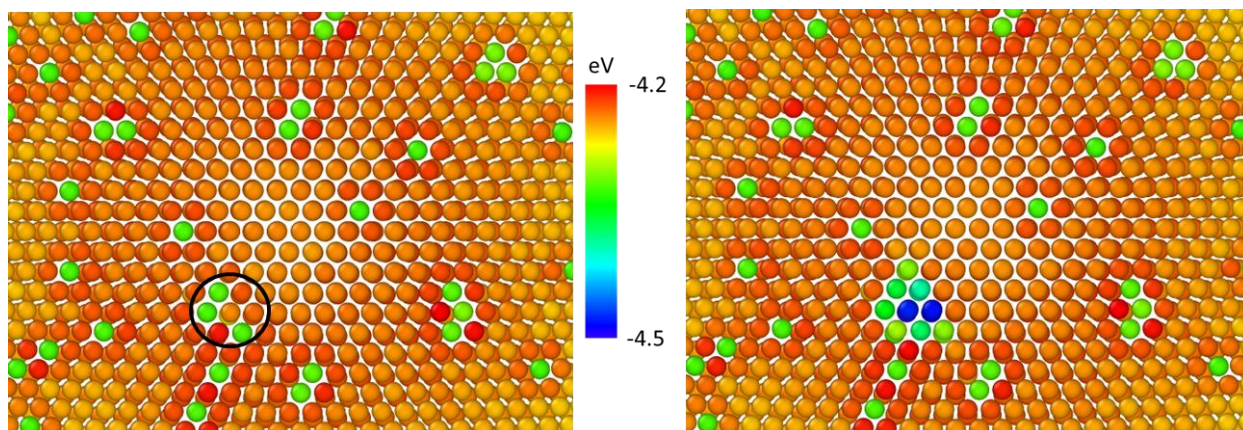


Figure 4.5 Top view of the phase transformation initiation in the membrane with a diameter of 100 nm and 0.05 point defect ratio. Mo atoms are removed and S atoms are colored by potential energy in both figures. Atoms colored green are the top S sulfur atom above a sulfur vacancy. A group of 3 vacancies, where the phase transformation initiates from, closest to the center of the membrane is marked by the black circle.

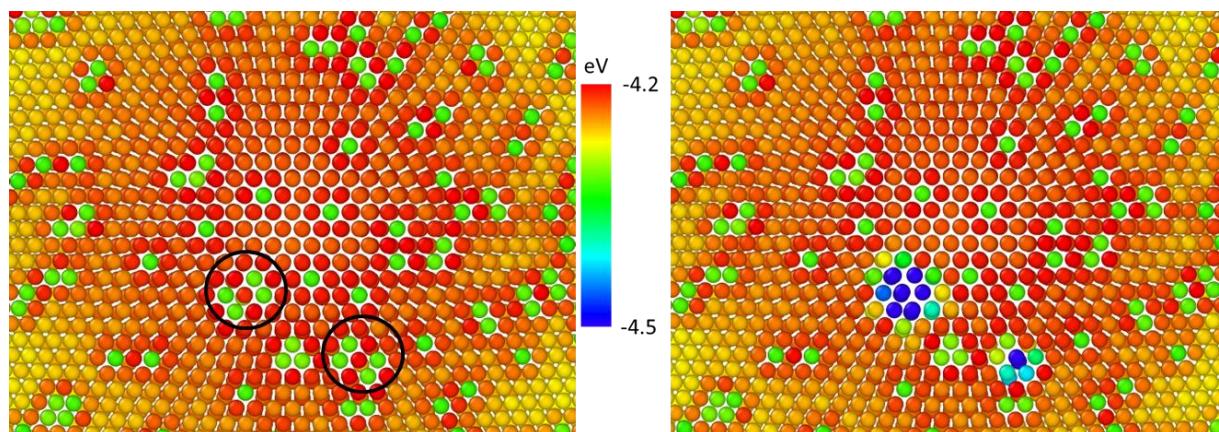


Figure 4.6 Top view of the phase transformation initiation in the membrane with a diameter of 200 nm and 0.1 point defect ratio. Mo atoms are removed and S atoms are colored by potential energy in both figures. Atoms colored green are the top S sulfur atom above a sulfur vacancy. Different groups of accumulated vacancies, where the phase transformation initiates from, are marked by the black circles.

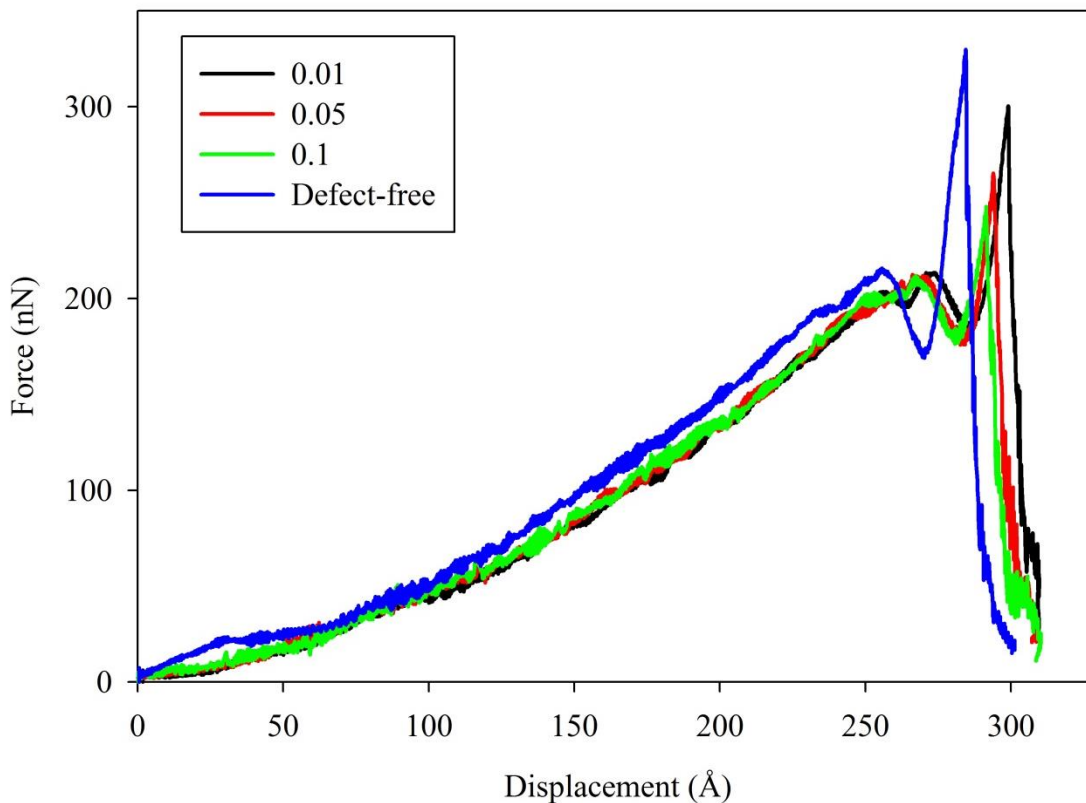


Figure 4.7 Force – displacement curve for nanoindentation on suspended circular monolayer MoS₂ membranes with and without monosulfur vacancies. The diameter of these membranes is 200 nm.

Table 4.3 Breaking forces for different membrane sizes and point defect ratios. Breaking forces are reported in nN.

D _{membrane}	GB structures			
	no defect	4 fold S	Mo bridge	4/8 ring
100 nm	324	297	268	239
150 nm	330	291	266	229
200 nm	329	290	256	219

4.3 Effect of different 60° grain boundary structures on mechanical behaviors of monolayer MoS₂

The grain boundary energy is plotted for all 10,000 relaxed structures constructed via molecular statics algorithm for all membrane sizes. Typical shapes of the data plots for 60°

armchair and zigzag symmetric tilt grain boundary structures are shown in Figure 4.8 and 4.9, respectively. Visual analysis via OVITO shows that there are two main structures of the 60° armchair symmetric tilt grain boundary corresponding to a grain boundary energy of approximately 0.44 and 0.65 to 0.82 eV/Å. As shown in Figure 4.10, the structure with the lowest grain boundary energy of 0.44 eV/Å composed of a line of S atom pairs where each S is surrounded with 4 instead of 3 Mo atoms (4-fold S) in normal hexagonal crystal structure. This structure along with the grain boundary energy is consistent with DFT calculations [63] and experimental observations [64]. The other 60° armchair symmetric tilt grain boundary composed Mo atom bridging (Mo-bridge) between two grains as shown in Figure 4.11. This structure was predicted via combined DFT and MD methods and observed experimentally by Enyashin *et al.* [65]. When brought to equilibrium at 600 K, there are Mo-Mo metallic bonds between the central Mo-bridge similar to DFT calculations [65]. The structures with grain boundary energy greater than 0.82 eV/Å are various distorted version of the two main structures. There is only one structure observed for the 60° zigzag symmetric tilt grain boundary corresponding to the lowest grain boundary energy. As shown in Figure 4.12, it is composed of alternating 4/8 rings of Mo and S atoms (4/8 ring) similar to DFT predictions [64]. The grain boundary energy of this structure is 0.39 eV/Å, which is in agreement with DFT calculations performed by Zou *et al.* [63].

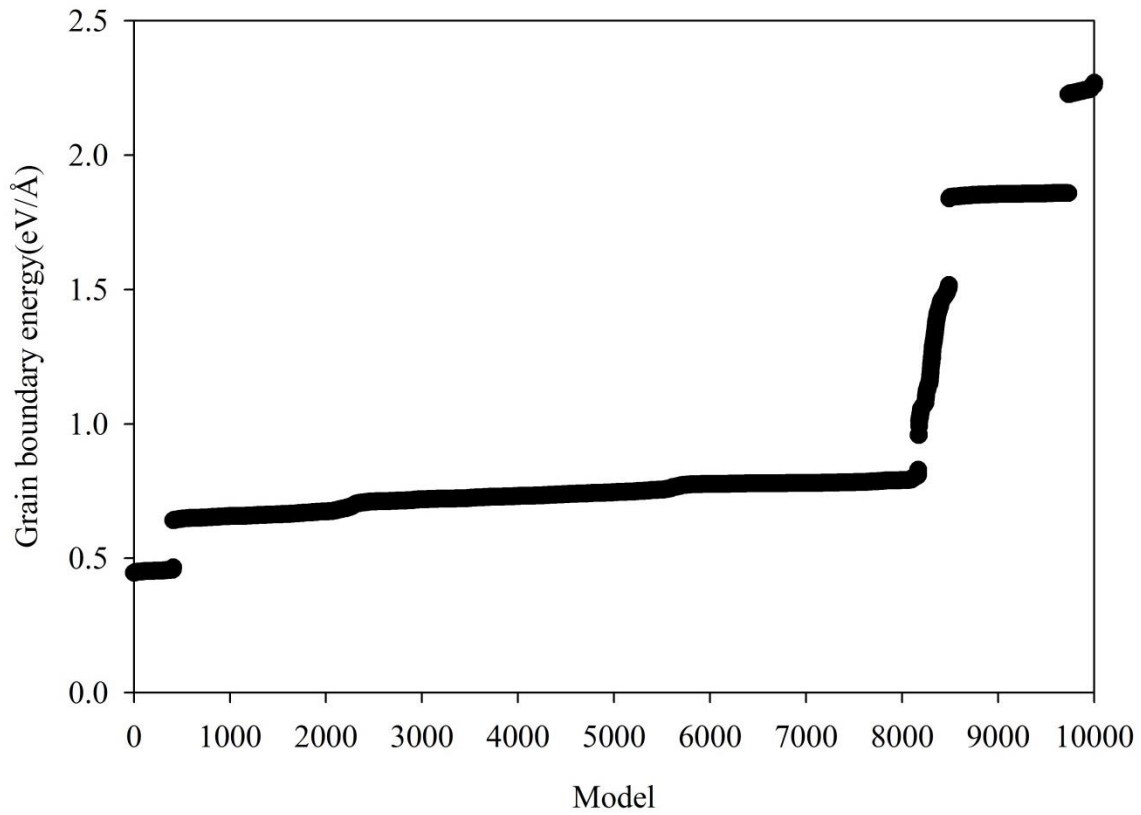


Figure 4.8 Grain boundary energies for 60° armchair symmetric tilt grain boundary structures of monolayer MoS₂ membrane with diameter of 100 nm.

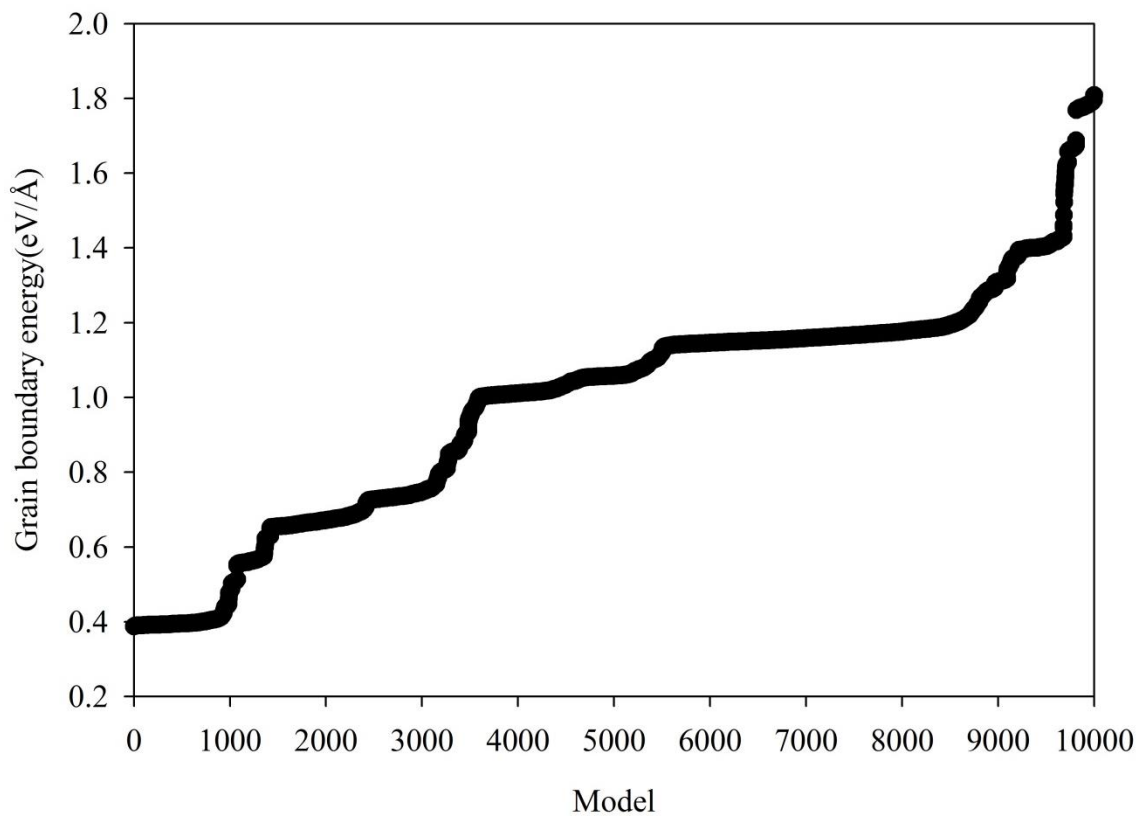


Figure 4.9 Grain boundary energies for 60° zigzag symmetric tilt grain boundary structures of monolayer MoS₂ membrane with diameter of 100 nm.

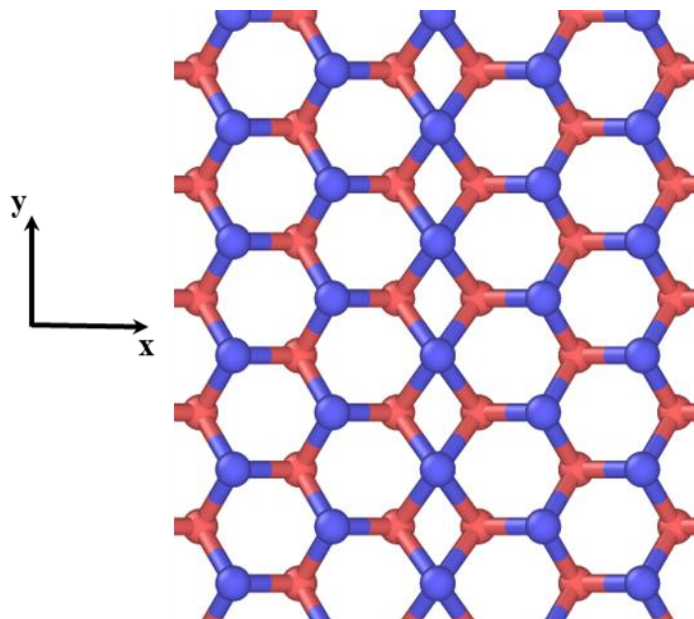


Figure 4.10 60° armchair symmetric tilt 4-fold S grain boundary structure of monolayer MoS_2 corresponding to grain boundary energy of $0.44 \text{ eV}/\text{\AA}$. Mo atoms are red, while S atoms are blue.

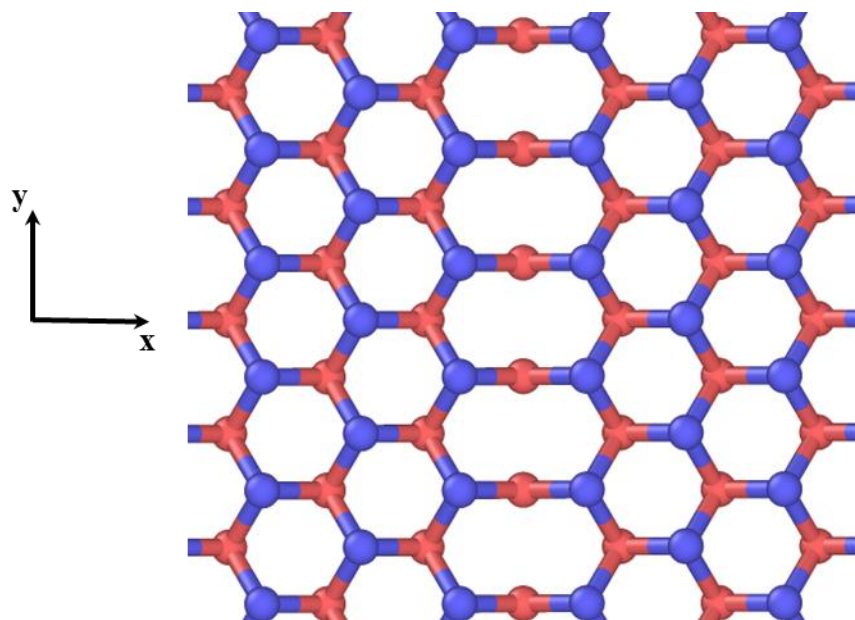


Figure 4.11 60° armchair symmetric tilt Mo-bridge grain boundary structure of monolayer MoS_2 corresponding to grain boundary energy range from 0.65 to $0.82 \text{ eV}/\text{\AA}$. Mo atoms are red, while S atoms are blue.

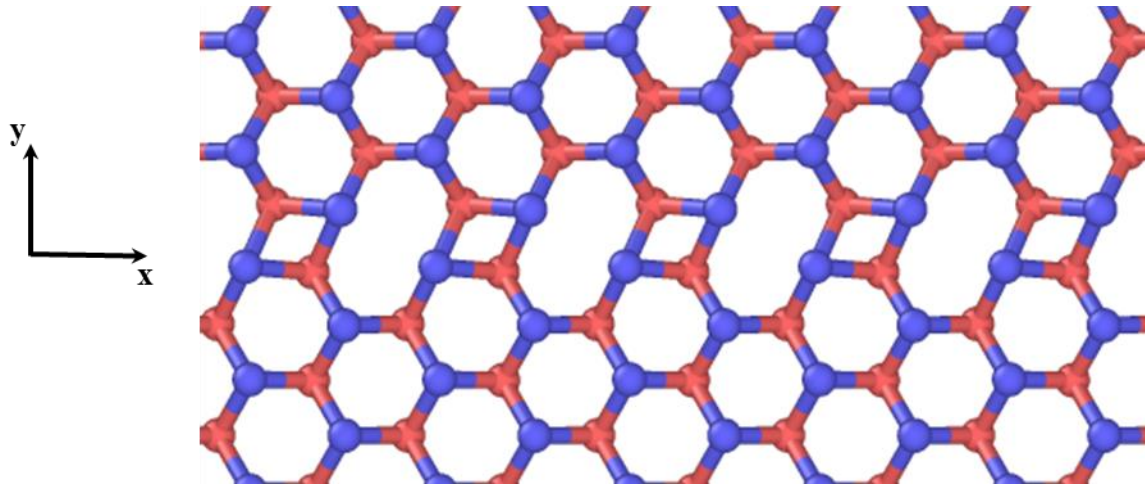


Figure 4.12 60° zigzag symmetric tilt 4/8 grain boundary structure of monolayer MoS_2 corresponding to grain boundary energy of $0.39 \text{ eV}/\text{\AA}$. Mo atoms are red, while S atoms are blue.

In Table 4.4, breaking forces from nanoindentation on the suspended circular monolayer of MoS_2 membranes with 60° symmetric tilt grain boundary structures are compared to corresponding defect-free membrane simulations from Chapter 3. In general, the 60° symmetric tilt grain boundary structures reduce the required breaking forces to fracture the monolayer MoS_2 membrane. Interestingly, the mechanical performance of these grain boundary structures is not proportional to the grain boundary energy. While the 4/8 ring grain boundary has the lowest grain boundary energy among the three structures, its breaking force is consistently the lowest for all membrane sizes. This indicates that the grain boundary energy is independent of how well the structure mechanically performs. As discussed in Chapter 3, the phase transformation is initiated with the S-S intralayer Z dimension distance drop from 3.1 \AA to 2.9 \AA . Similar phase transformation is observed in all 60° symmetric tilt grain boundary simulations. Depending on the grain boundary structures, this phase transformation occurs at different nanoindentation displacements, explaining the variation in breaking force among them. Among the three 60° symmetric tilt grain boundary structures, the 4-fold S grain boundary structure is the most packed, surrounded by 4 Mo atoms. Therefore, it is difficult to compress the central S atom pairs,

which is required to initiate the phase transformation that leads to failure. Indeed, the phase transformation in the 4-fold S grain boundary structure is initiated from but not within the grain boundary region. As shown in Figure 4.13, the phase transformation initiates from the 4 S pairs close to the grain boundary region with the S-S intralayer Z dimension distance drop from 3.1 Å to 2.9 Å. However, the S-S intralayer Z dimension distance of central S pairs within the grain boundary region still remains approximately 3.3 Å. Even though the phase transformation of Mo-bridge grain boundary structure also initiates from but not within the grain boundary structure, its mechanical performance is worse than the 4-fold S grain boundary structure due to the phase transformation propagation mechanism. Figure 4.14 compares the phase transformation propagation process of Mo-bridge and 4-fold S grain boundary structure. For Mo-bridge grain boundary membrane, once nucleated, the phase transformation propagates symmetrically outward. On the other hand, for 4-fold grain boundary membrane, the central 4-fold S atom pairs act as a barrier slowing down the phase transformation propagation, resulting in higher breaking force. Finally, the 4/8 ring grain boundary structure is the least packed among the three 60° symmetric tilt grain boundary structures. Therefore, it is relatively easy to compress the S atom pairs in this structure, resulting in the lowest required breaking force. Figure 4.15 captures the phase transformation in the 4-fold S grain boundary structure initiates with 3 S pairs within the grain boundary region. Similar to membranes with point defects, the breaking forces for the grain boundary membranes reduce for larger membranes, especially for the 4/8 ring grain boundary structure. For large membrane diameter, the curves of defect-containing membranes are shifted to the right relative to the curve of the defect-free membrane as shown in Figure 4.16, indicating localized deformation at the center of the membrane.

Table 4.4 Breaking forces for different membrane sizes and grain boundary structures. Breaking forces are reported in nN.

D _{membrane}	GB structures			
	no defect	4 fold S	Mo bridge	4/8 ring
100 nm	324	297	268	239
150 nm	330	291	266	229
200 nm	329	290	256	219

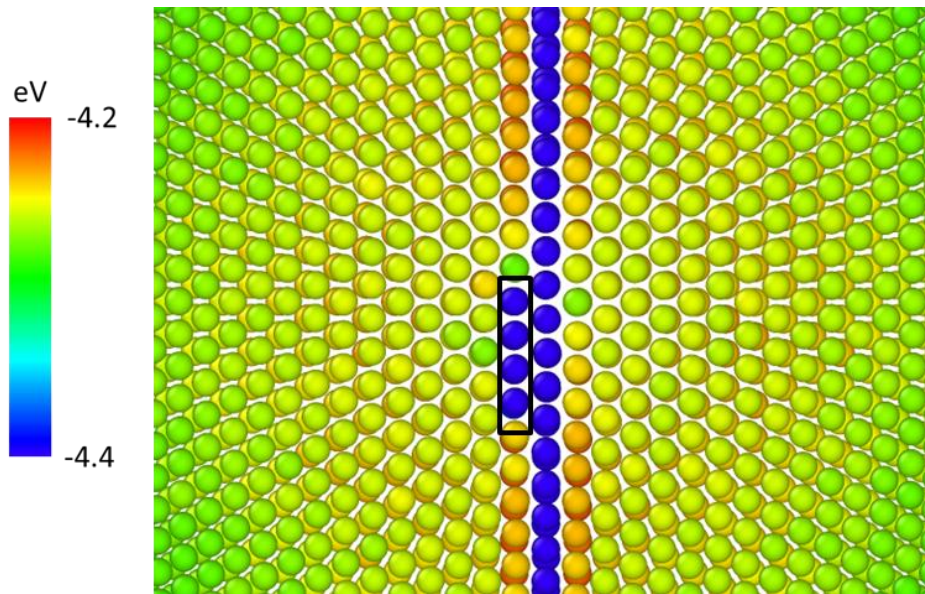


Figure 4.13 Top view of the phase transformation initiation in 4-fold S grain boundary membrane with diameter of 150 nm. Mo atoms are removed and S atoms are colored by potential energy in both figures. The black box marks 4 S pairs that initiate the phase transformation.

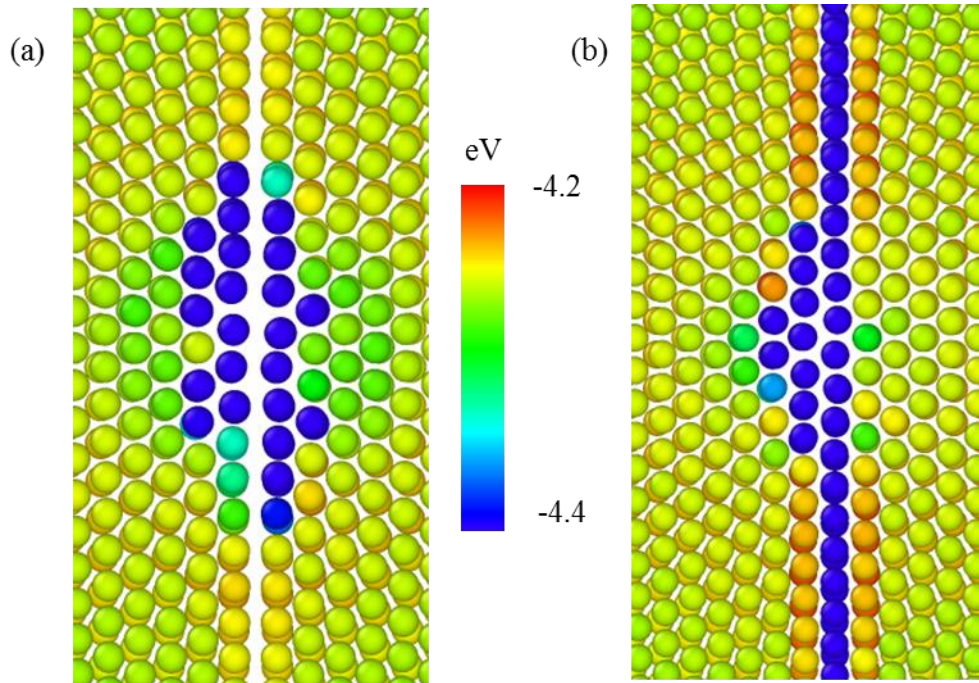


Figure 4.14 Top view of the phase transformation propagation process of Mo-bridge (a) and 4-fold S (b) grain boundary membrane with diameter of 100 nm. Mo atoms are removed and S atoms are colored by potential energy in both figures.

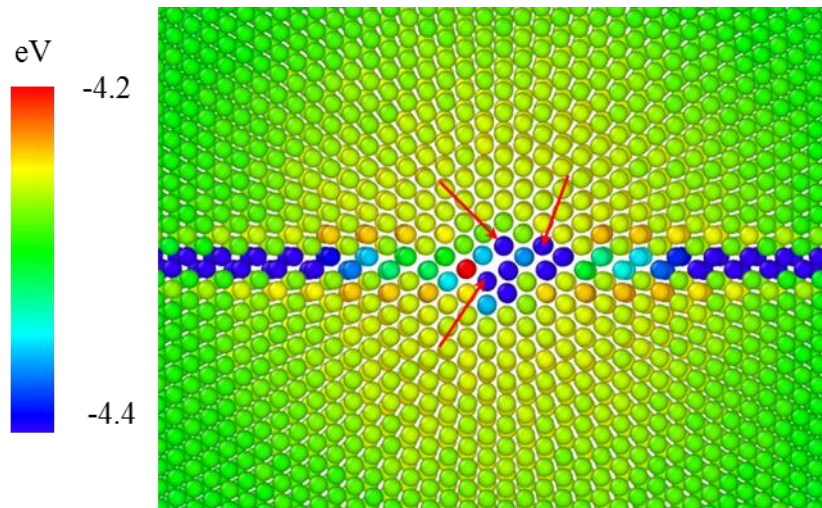


Figure 4.15 Top view of the phase transformation initiation in 4/8 ring grain boundary membrane with diameter of 150 nm. Mo atoms are removed and S atoms are colored by potential energy in both figures. The red arrows mark 3 S pairs that initiate the phase transformation.

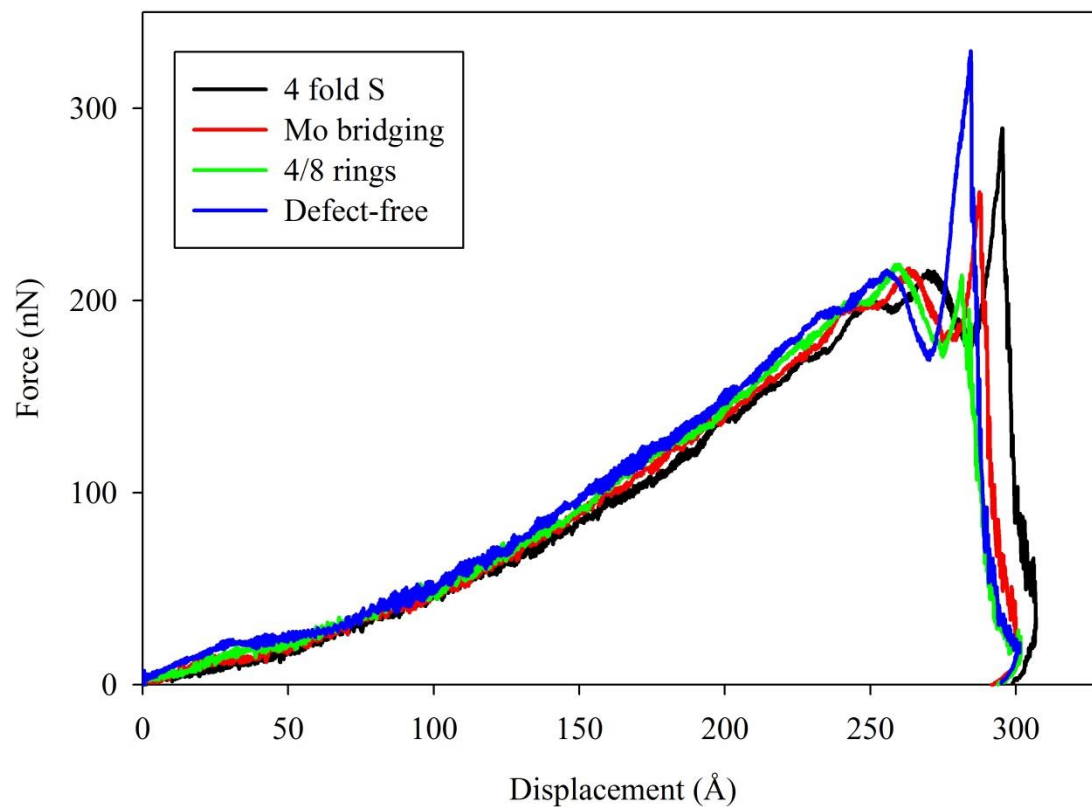


Figure 4.16 Force – displacement curve for nanoindentation on suspended circular monolayer MoS₂ membranes with and without grain boundary structures. The diameter of these membranes is 200 nm.

CHAPTER 5: CONCLUSION

5.1 Summary

Molecular dynamics simulations in this work utilized a REBO style interatomic potential that has been parameterized for Mo-S systems to study the mechanical properties and failure mechanisms of monolayer MoS₂ membranes under different tensile loading conditions.

“Nanoindentation was performed on suspended, free-standing membranes with different diameters to generate a mutiaxial tension deformation state analogous to experiments in the literature. The force required for fracture of the MoS₂ monolayer increases with increasing indenter diameter. This relationship and the magnitudes of the breaking forces computed in this work are consistent with experiments presented in the literature [51,53]. A phase transformation, caused by the S-S intralayer Z dimension distance drop, is observed prior to failure during both multiaxial and uniaxial tension simulations [26,91]. It has not been confirmed experimentally in monolayer MoS₂; however, an analogous phase transformation in bulk MoS₂ samples at high pressures has been reported in the literature” [26,93].

Also, structural defects such as point defects (monosulfur vacancy) and grain boundary structures (60° symmetric tilt grain) are introduced into the monolayer MoS₂ membrane via molecular statics simulations. Nanoindentation simulations via molecular dynamics simulation are then performed to study the role of these defects on the mechanical properties and failure mechanisms. Similar to defect-free membrane simulations, there is a phase transformation observed in the defective membrane simulations. From these simulations, it is shown that these structural defects modified the failure mechanisms of monolayer MoS₂ and thus reduced its mechanical performance. Combining the diminishing effects of the point defect and the grain boundary structure on the required breaking force, it is reasonable that the breaking forces of the perfect crystal monolayer MoS₂ membrane is overshoot when comparing to experimental values of small indenters in Figure 3.3. For point defects, the accumulation of vacancies promotes stress-concentration points, allowing the phase transformation to initiate away from the center of

the membrane and accelerate the new phase propagation process. For grain boundary structures, it is found that their mechanical performance is independent of the grain boundary energy.

5.2 Recommendations for future work

Based on the results of this study, there are several potential directions and approaches for future works. Depending on the requirements of certain applications, electronic devices made from bilayer MoS₂ is preferred due to its higher strength [51]. A supplemental simulation of nanoindentation on a defect-free bilayer MoS₂ circular membrane whose diameter is 100 nm is performed with an indenter diameter of 20 nm. The result from this simulation is consistent with data from experiment [51]. The fracture strength of the bilayer membrane is 557 nN, which is higher than corresponding monolayer membrane fracture strength of 324 nN. Recently, electronic properties of bilayer MoS₂ transistors have been explored [97,98]. The Mo-S interatomic potential [35,66,67] used in this work demonstrates to be very accurate in predicting mechanical properties of monolayer MoS₂ under tension. It would be interesting to study the mechanical behaviors and failure mechanisms of bilayer MoS₂ and compare them to results of monolayer MoS₂ in this thesis.

Moreover, this work only focuses on two specifically representative types of structural defects which are monosulfur vacancies and 60° symmetric tilt grain boundary structures. For point defects, there are 6 different types observed experimentally [64]. Aside from monosulfur vacancy, it is also essential to understand of how each of these point defects affects the properties of monolayer MoS₂. The grain boundary algorithm developed in this work could potentially be used to predict the grain boundary structures of different symmetric tilt grain systems and study the effects of these structures on properties of monolayer MoS₂.

REFERENCES

- [1] I. Tuomi, *First Monday* 7 (2002).
- [2] A.M. Ionescu, H. Riel, *Nature* 479 (2011) 329.
- [3] S.Z. Butler, S.M. Hollen, L. Cao, Y. Cui, J. a Gupta, H.R. Gutiérrez, T.F. Heinz, S.S. Hong, J. Huang, A.F. Ismach, E. Johnston-Halperin, M. Kuno, V. V Plashnitsa, R.D. Robinson, R.S. Ruoff, S. Salahuddin, J. Shan, L. Shi, M.G. Spencer, M. Terrones, W. Windl, J.E. Goldberger, *ACS Nano* 7 (2013) 2898.
- [4] R. Mas-Ballesté, C. Gómez-Navarro, J. Gómez-Herrero, F. Zamora, *Nanoscale* 3 (2011) 20.
- [5] Wang, K. Takada, A. Kajiyama, M. Onoda, Y. Michiue, Zhang, M. Watanabe, T. Sasaki, *Chem. Mater.* 15 (2003) 4508.
- [6] K. Watanabe, T. Taniguchi, *Int. J. Appl. Ceram. Technol.* 8 (2011) 977.
- [7] R. Gatensby, N. McEvoy, K. Lee, T. Hallam, N.C. Berner, E. Rezvani, S. Winters, M. O'Brien, G.S. Duesberg, *Appl. Surf. Sci.* 297 (2014) 139.
- [8] G. Gao, W. Gao, E. Cannuccia, J. Taha-Tijerina, L. Balicas, A. Mathkar, T.N. Narayanan, Z. Liu, B.K. Gupta, J. Peng, Y. Yin, A. Rubio, P.M. Ajayan, *Nano Lett.* 12 (2012) 3518.
- [9] B. Hunt, J.D. Sanchez-Yamagishi, a F. Young, M. Yankowitz, B.J. LeRoy, K. Watanabe, T. Taniguchi, P. Moon, M. Koshino, P. Jarillo-Herrero, R.C. Ashoori, *Science* 340 (2013) 1427.
- [10] Y. Shi, W. Zhou, A.-Y. Lu, W. Fang, Y.-H. Lee, A.L. Hsu, S.M. Kim, K.K. Kim, H.Y. Yang, L.-J. Li, J.-C. Idrobo, J. Kong, *Nano Lett.* 12 (2012) 2784.
- [11] A.K. Geim, I. V Grigorieva, *Nature* 499 (2013) 419.
- [12] M. Xu, T. Liang, M. Shi, H. Chen, *Chem. Rev.* 113 (2013) 3766.
- [13] C. Lee, X. Wei, J.W. Kysar, J. Hone, *Science* 321 (2008) 385.
- [14] E. Pop, V. Varshney, A.K. Roy, *MRS Bull.* 37 (2012) 1273.
- [15] J.-H. Chen, C. Jang, S. Xiao, M. Ishigami, M.S. Fuhrer, *Nat. Nanotechnol.* 3 (2008) 206.
- [16] J.-U. Lee, D. Yoon, H. Cheong, *Nano Lett.* 12 (2012) 4444.

- [17] K.S. Novoselov, A.K. Geim, S. V Morozov, D. Jiang, M.I. Katsnelson, I. V Grigorieva, S. V Dubonos, A.A. Firsov, *Nature* 438 (2005) 197.
- [18] K.S. Novoselov, Z. Jiang, Y. Zhang, S. V Morozov, H.L. Stormer, U. Zeitler, J.C. Maan, G.S. Boebinger, P. Kim, A.K. Geim, *Science* 315 (2007) 1379.
- [19] K. Kim, J.-Y. Choi, T. Kim, S.-H. Cho, H.-J. Chung, *Nature* 479 (2011) 338.
- [20] T. Martins, R. Miwa, A. da Silva, A. Fazzio, *Phys. Rev. Lett.* 98 (2007).
- [21] M.-W. Lin, C. Ling, Y. Zhang, H.J. Yoon, M.M.-C. Cheng, L.A. Agapito, N. Kioussis, N. Widjaja, Z. Zhou, *Nanotechnology* 22 (2011) 265201.
- [22] M. Han, B. Özyilmaz, Y. Zhang, P. Kim, *Phys. Rev. Lett.* 98 (2007) 206805.
- [23] Z.H. Ni, T. Yu, Y.H. Lu, Y.Y. Wang, Y.P. Feng, Z.X. Shen, *ACS Nano* 2 (2008) 2301.
- [24] A.K. Geim, K.S. Novoselov, *Nat. Mater.* 6 (2007) 183.
- [25] P.A. Young, *J. Phys. D. Appl. Phys.* 1 (1968) 936.
- [26] K.Q. Dang, J.P. Simpson, D.E. Spearot, *Scr. Mater.* 76 (2014) 41.
- [27] W.O. Winer, *Wear* 10 (1967) 422.
- [28] R.E. Bell, R.E. Herfert, *J. Am. Chem. Soc.* 79 (1957) 3351.
- [29] R. Holinski, J. Gänshemer, *Wear* 19 (1972) 329.
- [30] M. Chhowalla, G. Amaratunga, *Nature* 407 (2000) 164.
- [31] Y. Epshteyn, T. Risdon, in: *12 Lubr. Grease Conf.*, 2010.
- [32] K.H. Hu, M. Liu, Q.J. Wang, Y.F. Xu, S. Schraube, X.G. Hu, *Tribol. Int.* 42 (2009) 33.
- [33] A. Shankara, P.L. Menezes, K.R.Y. Simha, S. V. Kailas, *Sadhana* 33 (2008) 207.
- [34] W. Zhang, D. Demydov, M.P. Jahan, K. Mistry, A. Erdemir, A.P. Malshe, *Wear* 288 (2012) 9.
- [35] J.A. Stewart, D.E. Spearot, *Model. Simul. Mater. Sci. Eng.* 21 (2013) 045003.
- [36] P. Joensen, R.F. Frindt, S.R. Morrison, *Mater. Res. Bull.* 21 (1986) 457.
- [37] B. Radisavljevic, A. Radenovic, J. Brivio, V. Giacometti, A. Kis, *Nat. Nanotechnol.* 6 (2011) 147.

- [38] A. Splendiani, L. Sun, Y. Zhang, T. Li, J. Kim, C.-Y. Chim, G. Galli, F. Wang, *Nano Lett.* 10 (2010) 1271.
- [39] K.F. Mak, C. Lee, J. Hone, J. Shan, T.F. Heinz, *Phys. Rev. Lett.* 105 (2010) 136805.
- [40] O. Lopez-Sanchez, D. Lembke, M. Kayci, A. Radenovic, A. Kis, *Nat. Nanotechnol.* 8 (2013) 497.
- [41] Z. Yin, H. Li, H. Li, L. Jiang, Y. Shi, Y. Sun, G. Lu, Q. Zhang, X. Chen, H. Zhang, *ACS Nano* 6 (2012) 74.
- [42] J. Lee, Z. Wang, K. He, J. Shan, P.X.-L. Feng, *ACS Nano* 7 (2013) 6086.
- [43] K. Lee, R. Gatensby, N. McEvoy, T. Hallam, G.S. Duesberg, *Adv. Mater.* 25 (2013) 6699.
- [44] B. Radisavljevic, M.B. Whitwick, A. Kis, *Appl. Phys. Lett.* 101 (2012) 043103.
- [45] B. Radisavljevic, M.B. Whitwick, A. Kis, *ACS Nano* 5 (2011) 9934.
- [46] Q. Peng, S. De, *Phys. Chem. Chem. Phys.* 15 (2013) 19427.
- [47] T. Li, *Phys. Rev. B* 85 (2012).
- [48] H.J. Conley, B. Wang, J.I. Ziegler, R.F. Haglund, S.T. Pantelides, K.I. Bolotin, *Nano Lett.* 13 (2013) 3626.
- [49] W.S. Yun, S.W. Han, S.C. Hong, I.G. Kim, J.D. Lee, *Phys. Rev. B* 85 (2012) 033305.
- [50] T.J. Mackin, P.J. Vernon, M.R. Begley, *Polym. Compos.* 25 (2004) 442.
- [51] S. Bertolazzi, J. Brivio, A. Kis, *ACS Nano* 5 (2011) 9703.
- [52] A.A. Griffith, *Philos. Trans. R. Soc. A Math. Phys. Eng. Sci.* 221 (1921) 163.
- [53] R.C. Cooper, C. Lee, C. a. Marianetti, X. Wei, J. Hone, J.W. Kysar, *Phys. Rev. B* 87 (2013) 035423.
- [54] J.-W. Jiang, H.S. Park, T. Rabczuk, *J. Appl. Phys.* 114 (2013) 064307.
- [55] O. V Yazyev, S.G. Louie, *Nat. Mater.* 9 (2010) 806.
- [56] S. Najmaei, Z. Liu, W. Zhou, X. Zou, G. Shi, S. Lei, B.I. Yakobson, J.-C. Idrobo, P.M. Ajayan, J. Lou, *Nat. Mater.* 12 (2013) 754.
- [57] A.M. van der Zande, P.Y. Huang, D. a Chenet, T.C. Berkelbach, Y. You, G.-H. Lee, T.F. Heinz, D.R. Reichman, D. a Muller, J.C. Hone, *Nat. Mater.* 12 (2013) 554.

- [58] J.C. Meyer, A. Chuvilin, G. Algara-Siller, J. Biskupek, U. Kaiser, *Nano Lett.* 9 (2009) 2683.
- [59] C. Jin, F. Lin, K. Suenaga, S. Iijima, *Phys. Rev. Lett.* 102 (2009) 195505.
- [60] R. Ansari, S. Ajori, B. Motevalli, *Superlattices Microstruct.* 51 (2012) 274.
- [61] J.-H. Chen, L. Li, W.G. Cullen, E.D. Williams, M.S. Fuhrer, *Nat. Phys.* 7 (2011) 535.
- [62] H.-P. Komsa, J. Kotakoski, S. Kurasch, O. Lehtinen, U. Kaiser, A. V. Krasheninnikov, *Phys. Rev. Lett.* 109 (2012) 035503.
- [63] X. Zou, Y. Liu, B.I. Yakobson, *Nano Lett.* 13 (2013) 253.
- [64] W. Zhou, X. Zou, S. Najmaei, Z. Liu, Y. Shi, J. Kong, J. Lou, P.M. Ajayan, B.I. Yakobson, J.-C. Idrobo, *Nano Lett.* 13 (2013) 2615.
- [65] A.N. Enyashin, M. Bar-Sadan, L. Houben, G. Seifert, *J. Phys. Chem. C* 117 (2013) 10842.
- [66] T. Liang, S. Phillpot, S. Sinnott, *Phys. Rev. B* 79 (2009) 245110.
- [67] T. Liang, S.R. Phillpot, S.B. Sinnott, *Phys. Rev. B* 85 (2012) 199903.
- [68] M.P. Allen, D.J. Tildesley, *Computer Simulation of Liquids*, Clarendon Press, Oxford, 1987.
- [69] D. Frenkel, B. Smit, *Understanding Molecular Simulation from Algorithms to Applications*, Academic Press, San Diego, 2002.
- [70] R. Lesar, *Introduction to Computational Materials Science Fundamentals to Applications*, University Press, Cambridge, 2013.
- [71] M.P. Allen, in: *Comput. Soft Matter From Synth. Polym. to Proteins*, Lect. Notes, 2004, pp. 1–28.
- [72] F. Ercolessi, *A Molecular Dynamics Primer*, 1997.
- [73] E.R. Hernandez, in: *Front. Contemp. Phys.*, 2008, pp. 95–123.
- [74] S. Plimpton, *J. Comput. Phys.* 117 (1995) 1.
- [75] A. Stukowski, *Model. Simul. Mater. Sci. Eng.* 18 (2010) 015012.
- [76] S. Melchionna, G. Ciccotti, B. Lee Holian, *Mol. Phys.* 78 (1993) 533.
- [77] W. Hoover, *Phys. Rev. A* 31 (1985) 1695.

- [78] J.R. Shewchuk, *Science* (80-.). 49 (1994) 64.
- [79] A.E. Carlsson, *Solid State Phys. Adv. Res. Appl.* 43 (1990) 1.
- [80] V. Alexiev, R. Prins, T. Weber, *Phys. Chem. Chem. Phys.* 2 (2000) 1815.
- [81] M.R. VanLandingham, *J. Res. Natl. Inst. Stand. Technol.* 108 (2003) 249.
- [82] C.A. Schuh, *Mater. Today* 9 (2006) 32.
- [83] I. Szlufarska, *Mater. Today* 9 (2006) 42.
- [84] Y. Zhong, T. Zhu, *Comput. Methods Appl. Mech. Eng.* 197 (2008) 3174.
- [85] K. Wasmer, R. Gassilloud, J. Michler, C. Ballif, *J. Mater. Res.* 27 (2011) 320.
- [86] C. Kelchner, S. Plimpton, J. Hamilton, *Phys. Rev. B* 58 (1998) 11085.
- [87] E.T. Lilleodden, J.A. Zimmerman, S.M. Foiles, W.D. Nix, *J. Mech. Phys. Solids* 51 (2003) 901.
- [88] C.P. Frick, T.W. Lang, K. Spark, K. Gall, *Acta Mater.* 54 (2006) 2223.
- [89] A.L. Kitt, Z. Qi, S. Rémi, H.S. Park, A.K. Swan, B.B. Goldberg, *Nano Lett.* 13 (2013) 2605.
- [90] A.J. Stone, D.J. Wales, *Chem. Phys. Lett.* 128 (1986) 501.
- [91] J. Simpsons, *Exploration into Properties of Molybdenum Disulfide Using Atomistic Simulation*, University of Arkansas, 2013.
- [92] J. Li, N. V. Medhekar, V.B. Shenoy, *J. Phys. Chem. C* 117 (2013) 15842.
- [93] R. Aksoy, Y. Ma, E. Selvi, M.C. Chyu, A. Ertas, A. White, *J. Phys. Chem. Solids* 67 (2006) 1914.
- [94] Y. Zhan, Z. Liu, S. Najmaei, P.M. Ajayan, J. Lou, *Small* 8 (2012) 966.
- [95] G. Cook, *Am. J. Phys.* 63 (1995) 737.
- [96] M. Bollinger, K. Jacobsen, J. Nørskov, *Phys. Rev. B* 67 (2003) 085410.
- [97] H. Wang, L. Yu, Y.-H. Lee, Y. Shi, A. Hsu, M.L. Chin, L.-J. Li, M. Dubey, J. Kong, T. Palacios, *Nano Lett.* 12 (2012) 4674.

- [98] M.M. Perera, M.-W. Lin, H.-J. Chuang, B.P. Chamlagain, C. Wang, X. Tan, M.M.-C. Cheng, D. Tománek, Z. Zhou, ACS Nano 7 (2013) 4449.